

Organic chemistry in the protosolar analogue HOPS-108: Environment matters

L. Chahine^{1,2}, A. López-Sepulcre^{1,3}, R. Neri¹, C. Ceccarelli³, S. Mercimek^{4,5}, C. Codella^{4,3}, M. Bouvier³,
E. Bianchi³, C. Favre³, L. Podio⁴, F. O. Alves⁶, N. Sakai⁷, and S. Yamamoto⁸

¹ Institut de Radioastronomie Millimétrique (IRAM), 300 rue de la Piscine, 38406 Saint-Martin-d'Hères, France
e-mail: chahine@iram.fr

² École doctorale de Physique, Université Grenoble Alpes, 110 Rue de la Chimie, 38400 Saint-Martin-d'Hères, France

³ Université Grenoble Alpes, CNRS, IPAG, 38000 Grenoble, France

⁴ INAF, Osservatorio Astrofisico di Arcetri, Largo E. Fermi 5, 50125, Firenze, Italy

⁵ Università degli Studi di Firenze, Dipartimento di Fisica e Astronomia, Via G. Sansone 1, 50019 Sesto Fiorentino, Italy

⁶ Center for Astrochemical Studies, Max Planck Institute for Extraterrestrial Physics, Garching, 85748, Germany

⁷ The Institute of Physical and Chemical Research (RIKEN), Saitama 351-0198, Japan

⁸ Department of Physics, The University of Tokyo, Bunkyo-ku, Tokyo 113-0033, Japan

Received 16 July 2021 / Accepted 13 October 2021

ABSTRACT

Context. Hot corinos are compact regions around solar-mass protostellar objects that are very rich in interstellar Complex Organic Molecules (iCOMs). How the abundance of these molecules is affected by the environmental physical conditions is still an open question. More specifically, addressing this point is key to understand our own chemical origins since the Solar System formed in a large cluster of low- to high-mass stars and was therefore subject to external heating and ultraviolet irradiation which may have shaped the chemistry of its early formation stages.

Aims. The goal of this high resolution study is to determine the abundance ratios of iCOMs in HOPS-108, which is a Class 0 protostar and a hot corino candidate located in the nearest Solar System analogue, the protostellar cluster OMC-2 FIR 4, in Orion. We aim to compare the abundance ratios to those found in other hot corinos, which are all located in less crowded environments, in order to understand the impact of environmental conditions on hot corinos' chemistry.

Methods. We observed the OMC-2 FIR 4 proto-cluster using the Band 6 of the Atacama Large (sub-)Millimetre Array in Cycle 4 with an angular resolution of $\sim 0''.28$ (110 au). We determined the abundances and temperature of the species using local thermodynamic equilibrium (LTE) and non-LTE analysis.

Results. Our results reveal a rich organic chemistry towards HOPS-108, asserting that it is a hot corino where the following iCOMs are detected: CH_3OH , HCOOCH_3 , CH_3OCH_3 , $\text{CH}_3^{18}\text{OH}$, CH_2DOH , CH_3COCH_3 , CH_3CHO , CH_3CN , $^{13}\text{CH}_3\text{CN}$, $\text{C}_2\text{H}_5\text{CN}$, and NH_2CHO . Remarkably, we find a possible enhancement in the HCOOCH_3 abundance with respect to other known hot corinos. Indeed, the $[\text{CH}_3\text{OCH}_3]/[\text{HCOOCH}_3]$ abundance ratio in this source is ~ 0.2 and, within the uncertainties, it deviates from the known correlation marginally where $[\text{CH}_3\text{OCH}_3]/[\text{HCOOCH}_3] \sim 1$. A relatively low $[\text{CH}_2\text{DOH}]/[\text{CH}_3\text{OH}]$ abundance ratio of ~ 0.02 is also obtained, which is in agreement with that found in another Orion source, HH212, suggesting a higher gas temperature during the early phases of ice mantle formation.

Conclusions. The $[\text{CH}_3\text{OCH}_3]/[\text{HCOOCH}_3]$ and $[\text{CH}_2\text{DOH}]/[\text{CH}_3\text{OH}]$ abundance ratios in HOPS-108 might result from different physical conditions in the Orion molecular complex compared to other regions. The former ratio cannot be reproduced with current chemical models, highlighting the importance of improving the chemical networks with theoretical calculations. More hot corinos located in heavily clustered regions such as Orion should be targeted in order to measure these ratios and evaluate whether they are an environmental product or whether HOPS-108 is an exceptional hot corino overall.

Key words. astrochemistry – ISM: individual objects: OMC-2 FIR 4 – ISM: molecules – stars: formation

1. Introduction

The first stages of solar-mass star formation are known for their molecular richness. Indeed, at the centre of the protostellar envelopes, some protostars may host compact (≤ 100 au), hot (≥ 100 K) and dense ($\geq 10^7$ cm⁻³) regions called hot corinos (Ceccarelli 2004; Ceccarelli et al. 2007; Caselli & Ceccarelli 2012). These are very rich in interstellar Complex Organic Molecules (iCOMs), that is, C-bearing molecules containing at least six atoms (Herbst & van Dishoeck 2009; Ceccarelli et al. 2017; Jørgensen et al. 2020). Their large molecular complexity is probably inherited and reprocessed in the subsequent stages

throughout the formation of a Sun-like star (Caselli & Ceccarelli 2012). Hence, understanding the chemistry of hot corinos is a crucial key to shed light on the conditions that favoured the emergence of life on our planet.

So far, most of the studied hot corinos are either isolated or were born in loose protoclusters. In contrast, our Sun was born in a crowded cluster in the vicinity of massive stars rather than in isolation (Adams 2010; Pfalzner et al. 2015). It is also known that the Sun was subject to internal irradiation from energetic particles (> 10 MeV), whose imprint is seen in the products of short-lived radionuclides in meteoritic material today (Gounelle et al. 2013). However, it is not yet understood whether these

Table 1. Analysed ALMA spectral windows.

Spectral window label	Central frequency (GHz)	Bandwidth (MHz)	Velocity resolution (km s ⁻¹)	Beam ($''$)	Beam PA ($^{\circ}$)	Chan. rms (mJy beam ⁻¹)
Continuum high frequency	246.2	1875	1.2	0.32×0.27	107	1.3
Continuum low frequency	232.2	1875	1.3	0.51×0.27	109	2.0
NH ₂ CHO 12 _{1,12} -11 _{1,11}	243.5	58.59	0.15	0.32×0.28	106	4.5
CH ₃ CN 14 ₀ -13 ₀	257.5	58.59	0.14	0.31×0.26	109	4.9
HCOOCH ₃ 24 _{1,24} -23 _{1,23}	259.3	58.59	0.14	0.31×0.26	106	3.7

conditions affected the early chemistry of the proto-Sun and its surroundings. From this standpoint, delving into the wide diversity of iCOMs in Solar-System-like environments is therefore fundamental to decipher the secret of our own origins. One of the best targets for this aim is OMC-2 FIR 4, a protostellar cluster located in the Orion Molecular Cloud 2, at a distance of 393 ± 25 pc (Grossschedl et al. 2018). It has a total mass of $30 M_{\odot}$ approximately (Mezger et al. 1990; Crimier et al. 2009) and a bolometric luminosity $\leq 1000 L_{\odot}$ (Crimier et al. 2009; Furlan et al. 2014). Due to various properties, it is thought to be the closest analogue to the environment in which the Sun may have been born. To begin with, OMC-2 FIR 4 is a young protocluster in which both low- and intermediate-mass protostars are forming (Shimajiri et al. 2008; López-Sepulcre et al. 2013b; Kainulainen et al. 2017; Tobin et al. 2019). It is located near the Trapezium OB star cluster, which bathes it in far ultraviolet (FUV) radiation ($\sim 1500 G_0$ where G_0 is the FUV radiation field in Habing units; López-Sepulcre et al. 2013a). Finally, a stream of high-energy cosmic-ray-like particles pervades the protocluster, ionising the surrounding envelope at a pace of 4000 times higher than cosmic rays (CRs) in our Galaxy (Ceccarelli et al. 2014, 2019; Fontani et al. 2017; Favre et al. 2018). On that premise, OMC-2 FIR 4 is the perfect analogue in pursuing a chemistry similar to that of our Solar System's early days. Particularly, the hot corino candidate HOPS-108 (Tobin et al. 2019) located within this protocluster can provide us with important hints about the chemistry of the gas and dust envelope surrounding our proto-Sun.

In this work, we present the first dedicated chemical study on the iCOMs of HOPS-108. This was performed using high-resolution (110 au) Atacama Large (sub-)Millimetre Array (ALMA) data at 1.2 mm.

The article is structured as follows: in Sect. 2 we describe the observations. In Sect. 3, we present the continuum and molecular line maps, together with the line identification and the main results of the analysis. In Sect. 4, we discuss the results, and, finally, in Sect. 5 we summarise the conclusions.

2. Observations

OMC-2 FIR 4 was observed with ALMA during its Cycle 4 operations, between 25 October 2016 and 5 May 2017, as part of the project 2016.1.00376.S (PI: Ana López-Sepulcre). The observations were taken with Band 6 in the ranges 218–234 GHz and 243–262 GHz. The phase-tracking centre was $\alpha_{\text{ICRS}} = 05^{\text{h}}35^{\text{m}}26^{\text{s}}.97$, $\delta_{\text{ICRS}} = -05^{\circ}09'54''.50$ and the systemic velocity was set to $V_{\text{LSR}} = 11.4 \text{ km s}^{-1}$. For the lower-frequency, 45 antennas of 12 m were used in the C-5 configuration of the array, probing angular scales from $0''.19$ to $11''.2$. The integration time on source was ~ 9 min, and the primary beam size is $\sim 27''.1$. For the higher-frequency spectral configuration, 42 antennas of 12 m were used in the C-5 configuration of the array, probing angular

scales from $0''.21$ to $8''.2$. The integration time on source was ~ 19 min and the primary beam size is $\sim 25''.6$. For both spectral configurations, J0510+1800 and J0522-3627 were used for bandpass and flux calibration, and J0607-0834 and J0501-0159 were used for phase calibration. The absolute flux calibration uncertainty is estimated to be $<10\%$. In the present work, focussed on iCOMs, we have used the five spectral windows (spws) listed in Table 1.

The data calibration was performed using the standard ALMA calibration pipeline with the Common Astronomy Software Applications package (CASA¹, McMullin et al. 2007), while self-calibration, imaging, and data analysis were performed using the IRAM-GILDAS software package². The continuum images were produced by averaging line-free channels from the 1.875 GHz spectral windows at 232 GHz and 246 GHz in the visibility plane. The remaining effective bandwidths are 458.9 MHz and 218.8 MHz, respectively. Phase self-calibration was then performed on the continuum emission and the gain solutions were applied to the line cubes. Continuum subtraction was performed on the cubes in the visibility plane, before line imaging. The resulting synthesised clean beam and channel root-mean-square (rms) noise level for each spectral window are summarised in Table 1.

3. Analysis and results

3.1. Continuum emission

Figure 1 shows the map of continuum emission at 246.2 GHz (1.2 mm). This map is not corrected for the primary beam attenuation, but all the flux densities used in the analysis have been corrected accordingly. We detected seven compact cores that are labelled as follows: the sources names HOPS-370, HOPS-64, and HOPS-108 refer to the sources identified in the *Herschel* Orion Protostar Survey (HOPS, Furlan et al. 2016); VLA16 and VLA15 refer to the sources identified in Osorio et al. (2017); MGM-2297 refers to Megeath et al. (2012); and ALMA1 refers to the source recently identified in Tobin et al. (2019). In addition, we detected some extended emission tracing the envelope of the protocluster. The source HOPS-370 is associated with the OMC-2 FIR 3 region, MGM-2297 is probably a foreground source and has no direct association with OMC-2 FIR 3 (Tobin et al. 2019), while the other five cores belong to the OMC-2 FIR 4 region. As we report in the next section, among the five cores in OMC-2 FIR 4, only HOPS-108 displays rich iCOM emission at these wavelengths, making it the only clear hot corino present in the protocluster. In this context, our work is only focussed on this source. As shown in the map, the emission of HOPS-108 is compact at the resolution of our observations. We fitted it with a circular Gaussian function in the uv plane, and we obtained coordinates of RA (J2000) = $05^{\text{h}}35^{\text{m}}27^{\text{s}}.084$ and

¹ <https://casa.nrao.edu/>

² <http://www.iram.fr/IRAMFR/GILDAS/>

Table 2. Detected molecules towards HOPS-108 in this work and their derived parameters.

Molecule	$N_{\text{lines}}^{(a)}$	E_{up} (K)	$T^{(b)}$ (K)	N_{tot} (cm^{-2})	$[X]/[\text{CH}_3\text{OH}]^{(e)}$ (%)	$[X]/[\text{HCOOCH}_3]^{(e)}$ (%)
LTE analysis						
HCOOCH ₃	28 [83]	49–366	96^{+3}_{-3}	$6.7^{+0.5}_{-0.5} \times 10^{17}$	4.8–13.4	=100
C ₂ H ₅ CN	6 [11]	161–285	145^{+62}_{-33}	$4.0^{+2.4}_{-1.5} \times 10^{15}$	0.03–0.08	$0.6^{+0.4}_{-0.2}$
CH ₂ DOH	1 [3]	113	100–150 ^(c)	$(1.5\text{--}2.5) \times 10^{17}$	1.0–5.0	/
CH ₃ COCH ₃	3 [10]	145–150	100–150 ^(c)	$(2.9\text{--}4.5) \times 10^{16}$	0.2–0.9	$5.5^{+1.3}_{-1.3}$
NH ₂ CHO	2 [2]	79	100–150 ^(c)	$(1.8\text{--}2.5) \times 10^{15}$	0.01–0.05	$0.3^{+0.1}_{-0.1}$
CH ₃ OCH ₃ ^(d)	3 [4]	81–174	100–150 ^(c)	$(0.7\text{--}2) \times 10^{17}$	0.5–4.0	$19.8^{+10.2}_{-10.2}$
CH ₃ CHO ^(d)	2 [3]	93	100–150 ^(c)	$(1.1\text{--}1.6) \times 10^{16}$	0.08–0.32	$2.0^{+0.4}_{-0.4}$
Non-LTE analysis						
CH ₃ OH	1 [9]	190–537	≥ 120	$0.5\text{--}1.4 \times 10^{19}$	=100	/
CH ₃ ¹⁸ OH ^(d)	5[6]	39–81	≥ 120	$0.9\text{--}2.5 \times 10^{16}$	=0.18	/
CH ₃ CN	2 [3]	93–100	120^{+30}_{-30}	$2.0^{+1.0}_{-1.0} \times 10^{16}$	0.1–0.4	$3.4^{+1.7}_{-1.7}$
¹³ CH ₃ CN	3 [5]	78–142	120^{+30}_{-30}	$4.0^{+1.0}_{-2.0} \times 10^{14}$	/	/

Notes. ^(a) Number of lines used in the analysis. The total number of detected transitions (i.e. including blends) is reported in brackets (see text). ^(b) T is the rotational temperature T_{rot} for HCOOCH₃ and C₂H₅CN, T_{ex} is that for the rest of molecules analysed using LTE, and T_{kin} is that for molecules analysed using non-LTE. ^(c) Adopted range of excitation temperatures (see Sect. 3.4). ^(d) Line flux measured after subtracting the small contribution from HCOOCH₃ and/or C₂H₅CN (see Sects. 3.3 and 3.4). ^(e) Abundance ratios of molecules marked as ‘/’ yield no meaningful information.

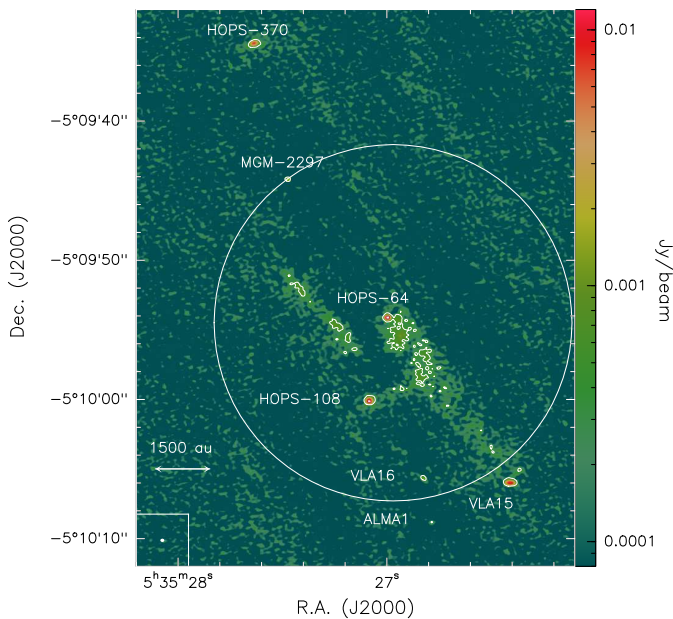


Fig. 1. Dust continuum emission map of OMC-2 FIR 4 at 1.2 mm. Contours at 5σ are shown with $\sigma = 95.7 \mu\text{Jy beam}^{-1}$. The different cores are labelled. The synthesised beam is depicted in white in the lower left corner. The primary beam at full width half maximum ($25''.6$) is depicted with a white circle.

Dec (J2000) = $-5^\circ 10' 00''.07$ consistent with those derived by Tobin et al. (2019), a source size of $0''.14$ (~ 55 au), and a flux density of $(20.0 \pm 0.1) \text{ mJy beam}^{-1}$.

3.2. Line identification and molecular maps

The line identification and analysis was performed using the extension WEEDS in the CLASS software of the GILDAS

package (Maret et al. 2011) using the Jet Propulsion Laboratory (JPL³, Pickett et al. 1998) and the Cologne Database for Molecular Spectroscopy (CDMS⁴, Müller et al. 2001, 2005) databases. The spectra were extracted from the central pixel corresponding to the position of the continuum emission peak. The line detection limit is set to 3σ at the intensity peak.

In terms of the line number, our spectra are dominated by HCOOCH₃, with more than 80 lines detected. We also detect between two and nine lines of CH₃OH, CH₃OCH₃, CH₃¹⁸OH, CH₂DOH, CH₃COCH₃, CH₃CHO, CH₃CN, ¹³CH₃CN, C₂H₅CN, and NH₂CHO. The detected transitions span over a large upper energy range ($E_{\text{up}} = 39\text{--}537$ K). The molecules are listed in Table 2. The line profiles were fitted with a Gaussian function with CLASS. The derived line parameters are summarised in Appendix A, and a sample of the observed lines for each detected molecule are shown in Figs. B.1–B.7. Moment 0 maps of the detected molecules are shown in Fig. 2. The emission is spatially compact. For all iCOMs, it peaks at the same position of the continuum peak (See Sect. 3.1).

The source size θ_s was obtained by stacking the uv tables of three HCOOCH₃ bright lines with the same velocity and full width at half-maximum (FWHM) in order to get a high signal-to-noise ratio (S/N) and then by fitting the emission in the stacked file with a circular Gaussian function in the visibility plane. The obtained value is $\theta_s = 0''.12 \pm 0''.02$ (~ 45 au), which is compatible with the value measured from continuum emission. The derived size was fixed to this value for the other molecules.

3.3. Non-LTE analysis

The collisional rates of CH₃OH and CH₃CN are available in the literature (Rabli & Flower 2010; Green 1986). To derive the physical properties of the gas emitting them, we performed a

³ <https://spec.jpl.nasa.gov>

⁴ <https://cdms.astro.uni-koeln.de>

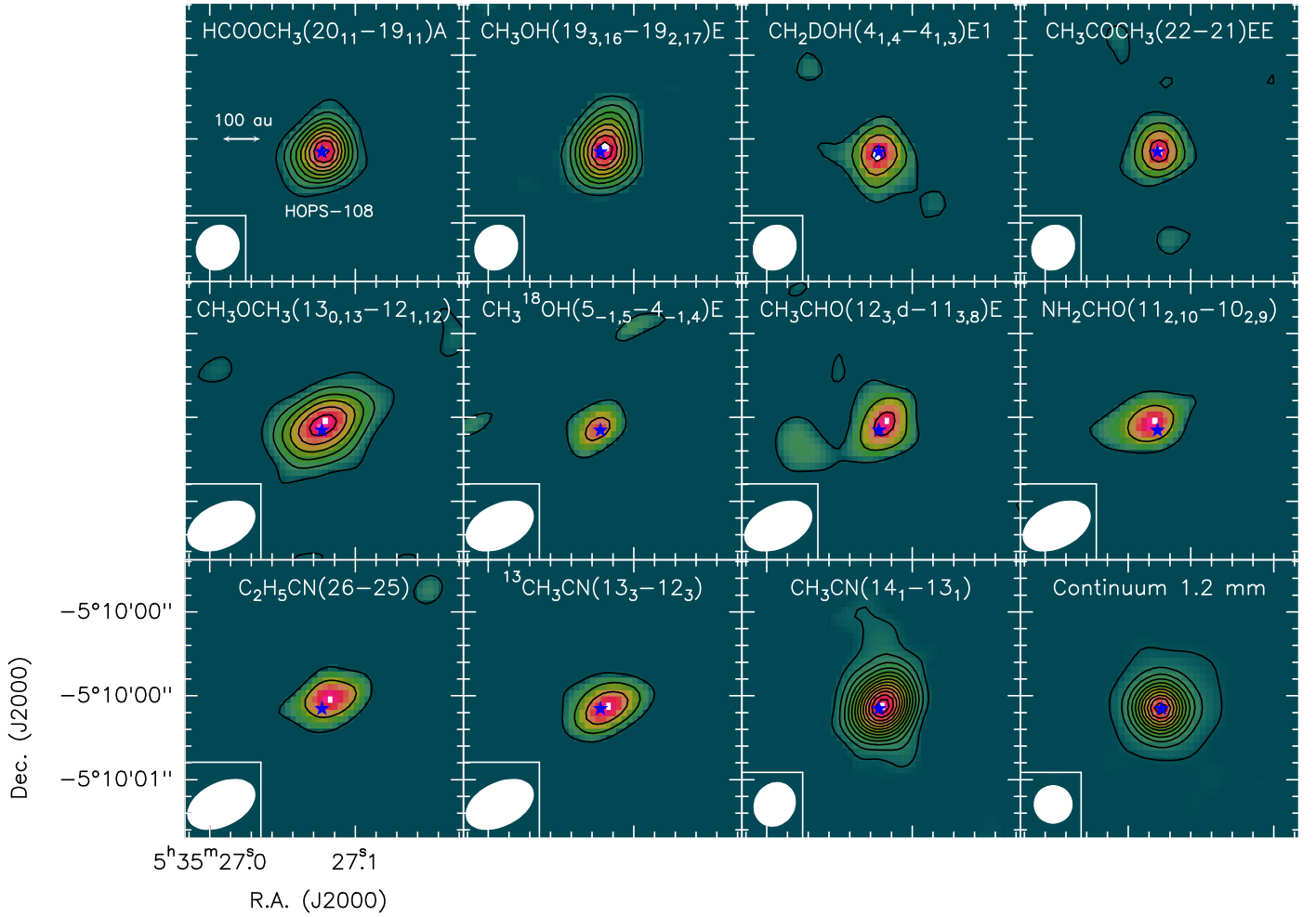


Fig. 2. Moment 0 maps of each detected molecule and of continuum emission towards HOPS-108. For CH_3OH and CH_3CN , contours start at 5σ and increase by steps of 5σ with $\sigma = 0.6 \text{ mJy km s}^{-1} \text{ beam}^{-1}$. For the other molecules, contours start at 3σ and increase by steps of 3σ with $\sigma = 0.6\text{--}1.1 \text{ mJy km s}^{-1} \text{ beam}^{-1}$. For the continuum emission, contours start at 5σ and increase by steps of 15σ with $\sigma = 95.7 \mu\text{Jy km s}^{-1} \text{ beam}^{-1}$. The synthesised beam is depicted in white in the lower left corner. The position of the continuum emission peak is depicted with a blue star.

non-local thermodynamic equilibrium (non-LTE) analysis using the large velocity gradient (LVG) code *grvelv* (Ceccarelli et al. 2003).

For CH_3CN and $^{13}\text{CH}_3\text{CN}$, we used the collisional coefficients with H_2 computed between 20 and 140 K by Green (1986) and provided by the LAMDA database (Schöier et al. 2005), which includes an extrapolation of the values for $T > 140 \text{ K}$. We assumed the $^{12}\text{C}/^{13}\text{C}$ ratio equal to 50 as obtained in the Orion OMC-2 region by Kahane et al. (2018). In our analysis, we included two CH_3CN lines, as the third is strongly blended with a HCOOCH_3 line, and three $^{13}\text{CH}_3\text{CN}$ lines, as the remaining two are also strongly blended with HCOOCH_3 lines.

We ran a large grid of models ($\geq 10\,000$) for both CH_3CN and $^{13}\text{CH}_3\text{CN}$, covering a range in column density $N_{\text{CH}_3\text{CN}}$ from 5×10^{15} to $3 \times 10^{17} \text{ cm}^{-2}$, which corresponds to a range of column density $N_{^{13}\text{CH}_3\text{CN}}$ from 1×10^{14} to $6 \times 10^{15} \text{ cm}^{-2}$, a H_2 density n_{H_2} from 3×10^5 to $6 \times 10^8 \text{ cm}^{-3}$, and a kinetic temperature T_{kin} from 50 to 200 K. Then, we fitted the $^{13}\text{CH}_3\text{CN}$ and CH_3CN lines simultaneously, leaving $N_{\text{CH}_3\text{CN}}$, $N_{^{13}\text{CH}_3\text{CN}}$, n_{H_2} , T_{kin} and the emitting size θ as free parameters. We assumed the line width equal to 2.5 km s^{-1} as measured (see Table A.1), and we included the calibration uncertainty (10%) and the rms errors in the uncertainty of the observed line intensities.

The best fit is obtained for $N_{\text{CH}_3\text{CN}} = 2 \times 10^{16} \text{ cm}^{-2}$ ($N_{^{13}\text{CH}_3\text{CN}} = 4 \times 10^{14} \text{ cm}^{-2}$) with a reduced chi-square $\chi_R^2 = 0.3$. The $^{13}\text{CH}_3\text{CN}$ lines are found to be optically thin ($\tau \sim 0.2$) while the CH_3CN lines are found to be optically thick ($\tau \sim 9$). The lines of the two isotopologues are emitted by a source of $0'.18$ in diameter. Their emitting size is more extended than that of HCOOCH_3 . Solutions with $1 \times 10^{16} \leq N_{\text{CH}_3\text{CN}} \leq 3 \times 10^{16} \text{ cm}^{-2}$ ($2 \times 10^{14} \leq N_{^{13}\text{CH}_3\text{CN}} \leq 6 \times 10^{14} \text{ cm}^{-2}$) are within 1σ of confidence level. Within the errors, the temperature is $(120 \pm 30) \text{ K}$ and the H_2 density is larger than $3 \times 10^7 \text{ cm}^{-3}$ at the 1σ confidence level.

For CH_3OH and $\text{CH}_3^{18}\text{OH}$, we used the collisional coefficients with H_2 computed between 10 and 200 K for the first 256 levels by Rabli & Flower (2010) and provided by the BASECOL database (Dubernet et al. 2013). We assumed the $^{18}\text{O}/^{16}\text{O}$ equal to 560 (Wilson & Rood 1994). To fit the LVG predictions, we included four $\text{CH}_3^{18}\text{OH}$ -e lines, two $\text{CH}_3^{18}\text{OH}$ -a lines, and one CH_3OH -e line. Among the other available eight CH_3OH lines, three have high upper level energies ($E_{\text{up}} \geq 400 \text{ K}$) and they were excluded from the analysis as the collisional coefficients are not computed at these energies. The other five lines have low excitation energies; they trace extended emission and hence they were excluded to avoid contamination. Among the available $\text{CH}_3^{18}\text{OH}$

lines, one is strongly blended with CH_2DOH and was excluded from the analysis, two are contaminated by a weaker line of HCOOCH_3 , and one is contaminated by $\text{C}_2\text{H}_5\text{CN}$, thus their integrated intensities were estimated after removing the expected intensity of the contaminating lines (see Appendix B). The spectrum is shown in Fig. B.6. For the CH_3OH line, the rms error was taken into account in the line flux. For $\text{CH}_3^{18}\text{OH}$, in addition to the rms error, we included the uncertainty of baseline imperfection due to rich spectra of iCOMs. We added an extra 20% in the flux error to account for the uncertainty linked to possible non-LTE effects.

As in the case of CH_3CN , we ran a large grid of models ($\geq 10\,000$) for both CH_3OH and $\text{CH}_3^{18}\text{OH}$, covering a range in column density $N_{\text{CH}_3\text{OH}}$ from 1×10^{16} to $7 \times 10^{19} \text{ cm}^{-2}$ that corresponds to a range in column density $N_{\text{CH}_3^{18}\text{OH}}$ from 2×10^{13} to $1.3 \times 10^{17} \text{ cm}^{-2}$, a H_2 density n_{H_2} from 8×10^6 to $2 \times 10^9 \text{ cm}^{-3}$, and a temperature T from 90 to 250 K. Then, we found the solution by simultaneously fitting the $\text{CH}_3^{18}\text{OH}$ -e and $\text{CH}_3^{18}\text{OH}$ -a lines as well as the CH_3OH -e line, leaving $N_{\text{CH}_3\text{OH}}$, $N_{\text{CH}_3^{18}\text{OH}}$, n_{H_2} , T_{kin} and the emitting size θ as free parameters. We assumed the $\text{CH}_3^{18}\text{OH}$ -e/ $\text{CH}_3^{18}\text{OH}$ -a ratio equal to 1, the line width equal to 3.6 km s^{-1} as measured (see Table A.1), and we included the uncertainties described in the previous paragraph in the observed intensities. While the comparison between the observations and model predictions constrain the CH_3OH and $\text{CH}_3^{18}\text{OH}$ column densities quite well (0.5×10^{19} – $1.4 \times 10^{19} \text{ cm}^{-2}$ and 0.9×10^{16} – $2.5 \times 10^{16} \text{ cm}^{-2}$, respectively), it does not allow one to put stringent limits on the density and temperature, other than the emitting gas temperature being larger than about 120 K and the density larger than about 10^6 cm^{-3} . The upper limits are even less constrained because the collisional coefficients are only available for $T \leq 200 \text{ K}$ and the levels become LTE-populated at about 10^6 cm^{-3} . The emitting size of CH_3OH and $\text{CH}_3^{18}\text{OH}$ is well constrained ($0''.10$ – $0''.12$) and it is consistent with that obtained from the analysis of the HCOOCH_3 lines. The $\text{CH}_3^{18}\text{OH}$ lines are found to be optically thin ($\tau \sim 0.1$) while the CH_3OH lines are found to be very optically thick ($\tau \sim 21$).

3.4. LTE analysis

For the iCOMs where collisional rates are not calculated, we assumed local thermodynamic equilibrium (LTE) conditions. Among these molecules, only two (HCOOCH_3 and $\text{C}_2\text{H}_5\text{CN}$) have a sufficiently large number of detected transitions spanning a large range of upper state energies, for which we could therefore build a rotational diagram (RD). In addition to the LTE assumption, to derive the column density and rotational temperature (T_{rot}) of these two molecules, we assumed optically thin emission. The upper level column density here is $N_u = (8\pi k\nu^2/hc^3 A_{ul})W$, where $W = \int T_B dV$ is the line integrated intensity and T_B is the brightness temperature.

To build the RD, we included the isolated lines, and the lines that consist of several transitions with the same upper level energy, but different Einstein coefficients and statistical weights as done by Bianchi et al. (2019). The blended lines were excluded from the analysis. The rms and calibration errors in the line fluxes were taken into account. The resulting rotational diagrams are shown in Fig. 3.

For HCOOCH_3 , we obtained a rotational temperature of $(96 \pm 3) \text{ K}$ and a column density of $(6.7 \pm 0.5) \times 10^{17} \text{ cm}^{-2}$. The lines with a high optical depth (>1) were excluded from the fit but are shown in the RD plot as lower limits, as a consistency

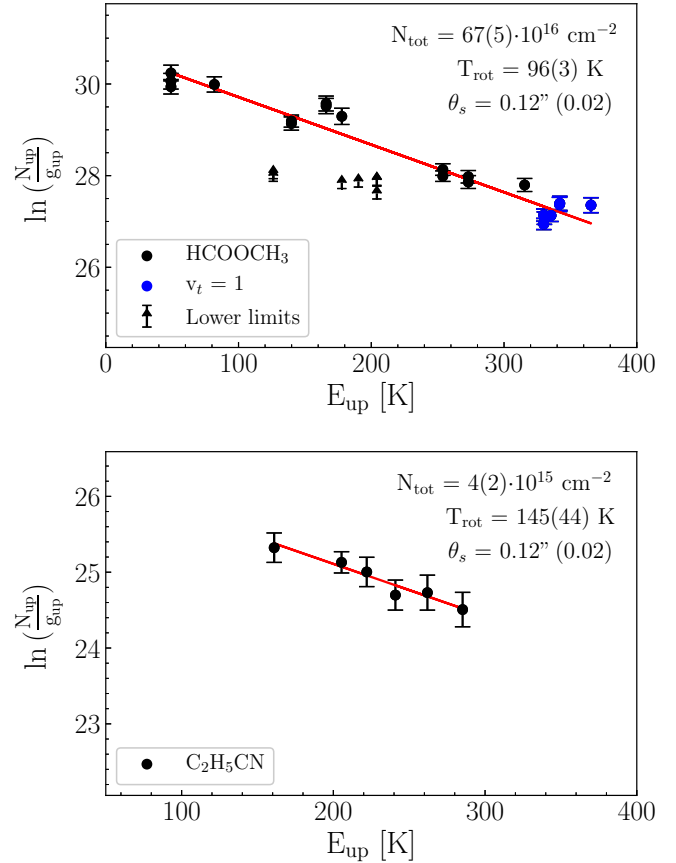


Fig. 3. Rotational diagrams for HCOOCH_3 (top) and $\text{C}_2\text{H}_5\text{CN}$ (bottom). Data points are presented in black. The $\text{HCOOCH}_3 v_t = 1$ transitions are depicted in blue. The arrow symbols represent the lower limits that are excluded from the analysis (see Sect. 3.4). The red lines correspond to the best fit to the data points.

check. For $\text{C}_2\text{H}_5\text{CN}$ we obtained a rotational temperature of $(145 \pm 44) \text{ K}$ and a column density of $(4.0 \pm 1.9) \times 10^{15} \text{ cm}^{-2}$.

For the other molecules, there are a few lines that cover a narrow E_{up} range, hence we calculated the column densities at an excitation temperature range $T_{\text{ex}} = 100$ – 150 K based on the derived rotational temperature for HCOOCH_3 and the kinetic temperature for CH_3OH (see Sect. 3.3). Also, here, we assumed LTE and optically thin line emission, and we took rms and calibration errors in the line fluxes into account. In our analysis, we included the unblended lines. We also included the lines that are slightly blended with HCOOCH_3 and/or $\text{C}_2\text{H}_5\text{CN}$ after subtracting the flux of the contaminant when it was estimated to be $<20\%$ of the total line flux (see Appendix B). Finally, we excluded the lines that are blended by other molecular species or strongly blended by either HCOOCH_3 or $\text{C}_2\text{H}_5\text{CN}$ ($>20\%$ of the total line flux).

More explicitly, for CH_2DOH , we included only one line as the other two are blended with $\text{CH}_3^{18}\text{OH}$ and CH_3COCH_3 . For CH_3COCH_3 , we included three lines as the others were either strongly blended with HCOOCH_3 , or with other molecular species. For NH_2CHO , we detected two isolated lines, which were both included in the analysis.

For CH_3OCH_3 , we detected four lines with emission higher than 5σ . One of them is likely blended with CH_2DCN , and it was excluded from the analysis. Another is very slightly contaminated with two weaker lines of HCOOCH_3 and $\text{C}_2\text{H}_5\text{CN}$, thus its line intensity was estimated after removing the expected

intensities of the contaminating lines (see Appendix B). The three available lines were not sufficient to build a RD, hence we derived the column density following the previously mentioned assumptions.

For CH₃CHO, we detected three lines, one of which is strongly blended with both CH₂DOH and HCOOCH₃, and two others are slightly blended with HCOOCH₃. We derived a column density value using the latter lines after removing the expected intensities of the contaminating HCOOCH₃.

The derived column densities of these iCOMs are summarised in Table 2.

4. Discussion

4.1. The hot corino in OMC-2 FIR 4

The OMC-2 FIR 4 region was extensively studied at large scales with the *Herschel* Space Observatory (López-Sepulcre et al. 2013a; Kama et al. 2013, 2015; Furlan et al. 2014; Ceccarelli et al. 2014; González-García et al. 2016; Fontani et al. 2017; Favre et al. 2017). At scales of $\sim 5''$, these studies provided a rather complete overview on FIR 4 and the surroundings. For example, it was found that the outer shell of OMC-2 FIR 4 is strongly irradiated by a FUV field ($\sim 1500 G_0$), arising from the high-mass stars located in the nearby Trapezium OB association (López-Sepulcre et al. 2013a). In addition, it was discovered that the interior envelope of FIR 4 is subject to irradiation and ionisation by local CR-like particles with an ionisation rate of $\zeta = 4 \times 10^{-14} \text{ s}^{-1}$ (Ceccarelli et al. 2014). Further interferometric studies at millimetre and sub-millimetre wavelengths with $\sim 1''\text{--}3''$ angular resolution revealed that OMC-2 FIR 4 is a protocluster harbouring several cores (Shimajiri et al. 2008; López-Sepulcre et al. 2013b; Kainulainen et al. 2017). They also confirmed the presence of FUV irradiation (López-Sepulcre et al. 2013b; Favre et al. 2018) and that of CR-like particles (Fontani et al. 2017; Favre et al. 2018). At sub-arcsecond resolution, in addition to the present work, the only available study to our knowledge was performed by Tobin et al. (2019). These authors characterised the protostellar content in OMC-2 FIR 4 by studying the dust continuum and methanol emission. In HOPS-108, they detected compact emission in CH₃OH, CH₃CN, and HCOOCH₃. From their three detected CH₃OH lines, they derived a rotational temperature of 140 K. While they reported that HOPS-108 is likely a hot corino, an extensive characterisation of its organic molecular content was out of their scope. In this context, our study is the most comprehensive one on iCOMs in this object. We detected a relatively large number of molecules that are typical tracers of hot corinos, including some that are more rarely detected even in such environments, such as CH₃COCH₃ and C₂H₅CN. All the detected molecules have compact emission centred on the continuum source (see Fig. 2). In addition, the majority of CH₃OH, HCOOCH₃, and C₂H₅CN lines we detected are highly excited ($E_{\text{up}} \geq 160 \text{ K}$ with a kinetic temperature of $\sim 150 \text{ K}$ and rotational temperature of $\sim 96 \text{ K}$ and 145 K , respectively), indicating that the emission originates from hot gas. This confirms that HOPS-108 is indeed a hot corino. From the HCOOCH₃ lines, we found that the systemic velocity of HOPS-108 is $\sim +12.3 \text{ km s}^{-1}$. From CH₃OH lines we found a systemic velocity of $\sim +12.6 \text{ km s}^{-1}$ which is equal to that obtained by Tobin et al. (2019), implying a redshift of $\sim 1.2 \text{ km s}^{-1}$ with respect to the ‘bulk’ velocity of the FIR 4 protocluster. It is worth noting that Kama et al. (2013) obtained an equal velocity from highly excited CH₃OH lines

($E_{\text{up}} = 450 \text{ K}$) at large scales with *Herschel* suggesting that also those lines primarily originated in HOPS-108.

4.2. Comparison with other hot corinos

The detection of a hot corino in what is currently considered to be the closest analogue of the Solar System birth environment naturally raises the question of how the chemistry of the hot corino is affected by the nearby massive stars and the internal source of high-energy particles. To this end, we compared iCOM abundances in HOPS-108 to those in other known hot corinos that are either isolated or located in loose protoclusters. In this comparison, we used the abundance ratios with respect to CH₃OH and HCOOCH₃, which are the most abundant molecules in hot corinos, and included data from low-mass Class 0 and Class I hot corinos obtained with (sub-)millimetre interferometers. We report the obtained abundance ratios in Table 2. Figure B.8 shows the column densities of the detected iCOMs normalised to that of CH₃OH where the sources are separated into Class 0 and I, and colour-coded according to the cloud where they are forming. For most of the molecules, a scatter of one order of magnitude is observed in the different abundance ratios. A larger scatter of almost two orders of magnitude is observed in the case of NH₂CHO and CH₃CHO. It is worth noting that similarly large differences in the iCOM abundance ratios across different hot corinos have been recently reported in several previous studies (Bergner et al. 2019; Bianchi et al. 2019; Belloche et al. 2020; Nazari et al. 2021). While these differences induce more complexities in the comparison of hot corinos, we can conclude that, within one order of magnitude, for most of the molecules, the abundance ratios in HOPS-108 are consistent with those found in other hot corinos, located in Perseus, Ophiuchus, and Serpens. They are also consistent with the ratios found in HH212, the other hot corino reported in Orion thus far. A different behaviour is shown by HCOOCH₃ and CH₂DOH, and they are described in the following subsections.

4.2.1. Abundance of methyl formate

Among all the iCOMs detected in HOPS-108, there is one that clearly stands out relative to other hot corinos, both in terms of line richness and column density: HCOOCH₃. Figure 4 shows the abundance ratios of HCOOCH₃ normalised to those of CH₃OH. The sources are separated according to their class and colour-coded depending on the star-forming region to which they belong. At first sight, the [HCOOCH₃]/[CH₃OH] ratio in HOPS-108 seems consistent with those found in other hot corinos. However, it is worth mentioning that the CH₃OH lines can be very optically thick towards hot corinos (Bianchi et al. 2020) and, therefore, in the majority of them, the column density of CH₃OH is underestimated unless it is derived from CH₃¹⁸OH or the ¹³CH₃OH isotopologue when the latter is optically thin. If we compare the [HCOOCH₃]/[CH₃OH] ratio for the sources where the CH₃OH column density is derived using one of the secondary isotopologues (filled symbols in Fig. 4), we can notice that the HCOOCH₃ is almost a factor of 3–5 more abundant in HOPS-108 with respect to other sources, pointing to a possible enhancement of HCOOCH₃ in this source. From the comparison of iCOM abundance ratios with respect to HCOOCH₃ in all of the sources (Fig. B.9), we can notice that within the errors, the N-bearing molecules ratios in HOPS-108 are lower than in other hot corinos, and those of O-bearing molecules are among the lowest, even though they are comparable to the values measured towards the IRAS 16293-2422 A and B sources. However, as

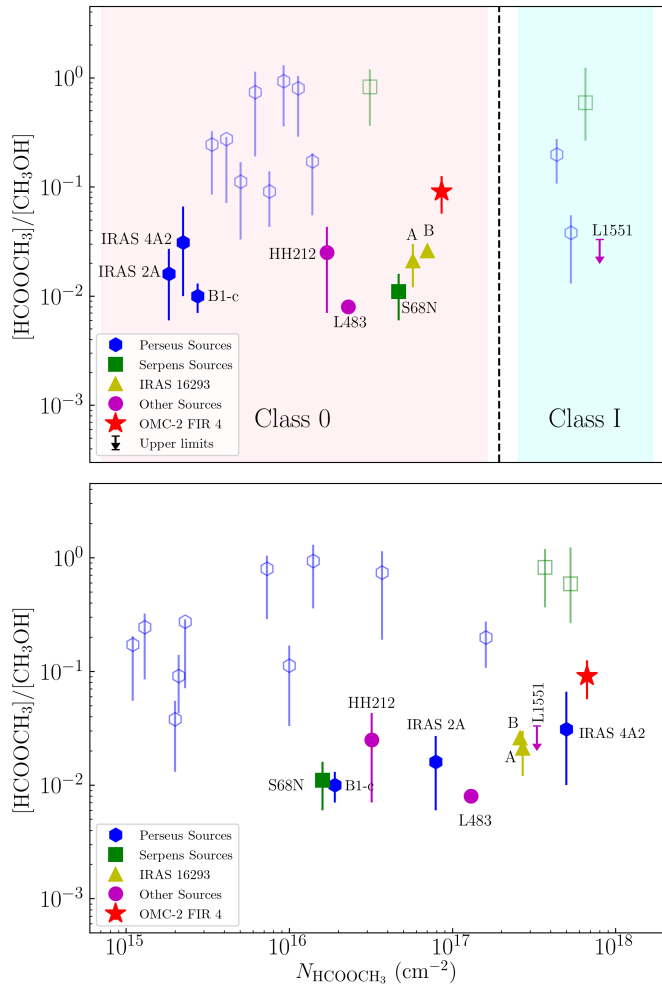


Fig. 4. Abundance ratio of HCOOCH_3 with respect to CH_3OH in HOPS-108 compared to other isolated hot corinos as a function of the class in no particular order within a given class (*top*) and HCOOCH_3 column density (*bottom*). The open symbols correspond to the sources where CH_3OH column density is most likely underestimated (see Sect. 4.2.1). The Class 0 sources are: IRAS 2A, IRAS 4A2 (Taqet et al. 2015; López-Sepulcre et al. 2017), B1-c, S68N (van Gelder et al. 2020), HH212 (Bianchi et al. 2017; Lee et al. 2019), L483 (Jacobsen et al. 2019), Ser-emb 1 (Bergner et al. 2019), IRAS 16293 A (Manigand et al. 2020), IRAS 16293 B (Jørgensen et al. 2016, 2018), HOPS-108 in OMC-2 FIR 4 (this work), and the sources from the PEACHES survey (Yang et al. 2021). The Class I sources are: Ser-emb 17 (Bergner et al. 2019), L1551 (Bianchi et al. 2020), and also sources from the PEACHES survey (Yang et al. 2021).

previously mentioned, the large scatters in the iCOM abundance ratios across the different hot corinos make the assessment challenging (Bergner et al. 2019; Bianchi et al. 2019; Belloche et al. 2020; Nazari et al. 2021).

An interesting result comes from the $[\text{CH}_3\text{OCH}_3]/[\text{HCOOCH}_3]$ abundance ratio which is lower in our source than in the other hot corinos, implying an enhancement in HCOOCH_3 . Intriguingly enough, the hot corino of OMC-2 FIR 4 is the only source that is marginally deviating within the errors from the well-known linear correlation between methyl formate (MF, HCOOCH_3) and dimethyl ether (DME, CH_3OCH_3), where $[\text{CH}_3\text{OCH}_3]/[\text{HCOOCH}_3] \sim 1$ (Fig. 5). This correlation was observed by Jaber et al. (2014) over a range of almost five orders of magnitude, with a Pearson correlation

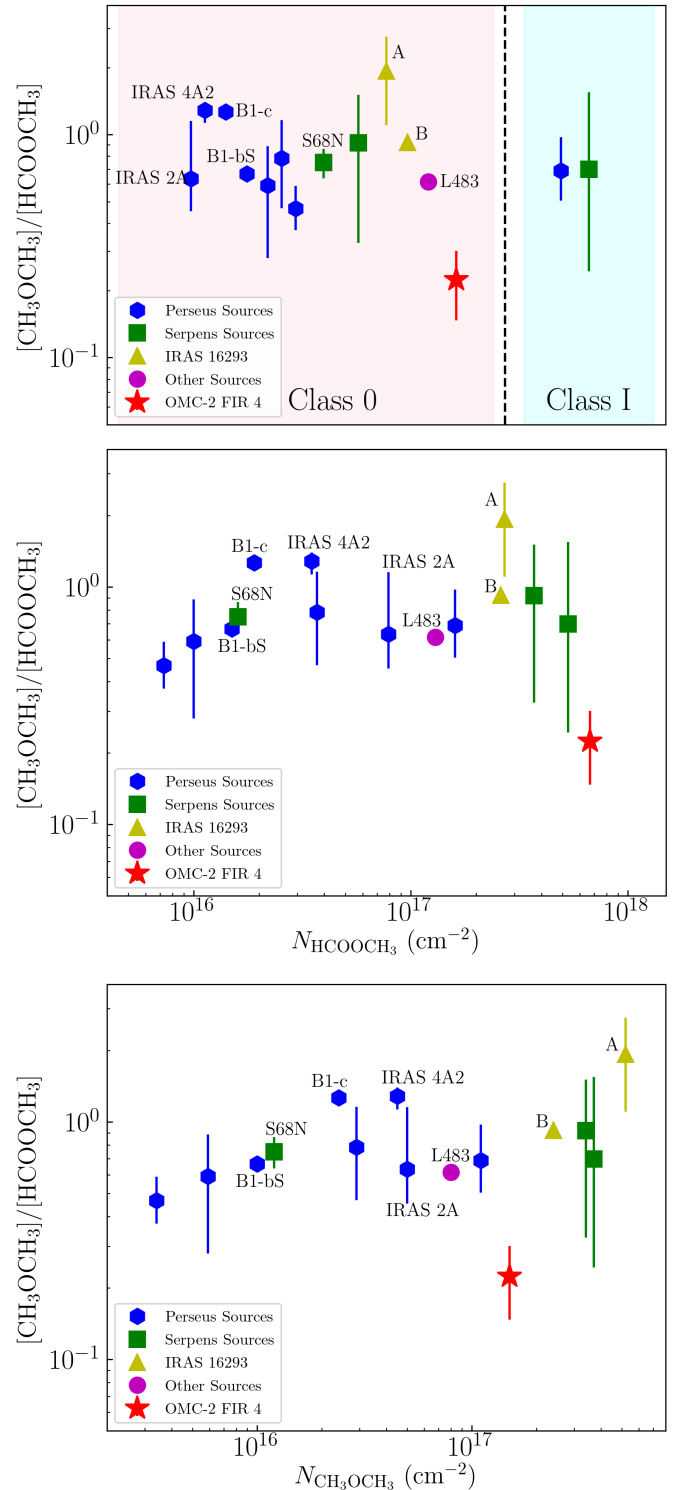


Fig. 5. Abundance ratio of CH_3OCH_3 with respect to HCOOCH_3 in HOPS-108 compared to other isolated hot corinos. In the *top plot*, the sources are separated according to their class, with no particular order within a given class. In the *middle and bottom plots*, the abundances are as a function of HCOOCH_3 and CH_3OCH_3 column densities, respectively. The same sources from Fig. 4 are used, including B1-bS (Marcelino et al. 2018).

coefficient equal to 0.95. It was also previously observed by Brouillet et al. (2013) over a smaller range. The MF-DME relation is well reproduced with the model by Balucani et al. (2015), using gas-phase reactions in cold environments. In

this model, MF is formed from DME via the oxidation of CH_3OCH_2 , while DME itself forms via the effective radiative association of the radicals CH_3 and CH_3O in the gas phase (see their Fig. 1). In what follows, we discuss two possibilities to explain the DME/MF abundance ratio found in HOPS-108: (i) an enhancement of CR ionisation in the gas phase, producing more MF and destroying DME, or (ii) a formation on the grain surface ‘through non-diffusive mechanisms’.

We tested the first possibility using a toy model by [Balucani et al. \(2015\)](#) at three values of the CR ionisation rate, ζ , using the kinetic temperature, the gas density, and the emitting size obtained from the non-LTE analysis of methanol. The results are shown in Fig. B.10. It can be seen that the formation and destruction of MF and DME still go almost hand in hand for the three ζ values. The model actually predicts a DME/MF ratio larger than unity for CRs enhanced regions (top panel) as well as an overall lower abundance of both molecules, while our results show a relatively low ratio and a large column density of both molecules. Thus, even with an enhancement of the CR ionisation rate, if we assume formation in the gas-phase, with the present gas-phase network, the model does not yield more MF than DME. This suggests that CR-like particles do not play a role in shaping the abundance of DME relative to that of MF. Alternatively, the chemical network may not be complete concerning the destruction routes of MF and DME, where the destruction of DME is supposed to be higher to match our observations. To clarify this point, we need new theoretical and experimental chemical calculations on these pathways. For example, by studying new experimental and theoretical calculations on the destruction of MF and DME by He^+ , [Ascenzi et al. \(2019\)](#) obtained reaction rate coefficients that are very different from those given by KIDA and UrdA databases, showing that this could impact the predicted abundances by 40% or even more depending on the physical conditions. This shows that the inclusion of correct reactions and rate coefficients in the astrochemical networks can have a crucial role in modelling and abundance predictions.

Regarding the second possibility, the model by [Jin & Garrod \(2020\)](#) is currently the one that approaches most of our observed MF column density value, but not that of DME. This model introduces new non-diffusive mechanisms for iCOM formation on grain surfaces. The one that comes closer to our MF value is called the three-body excited formation process (3-BEF), where radicals are formed in an excited state, allowing them to overcome activation barriers to react with nearby stable molecules. In this mechanism, MF is formed through the reaction of an excited CH_3O radical with CO on the grain surface producing CH_3OCO , which is converted to HCOOCH_3 by hydrogenation. This mechanism enhances the grain-surface production of MF which results in an abundance almost two orders of magnitude higher than that of DME. Nonetheless, it is unclear why this mechanism would affect the HOPS-108 hot corino and not other sources. In addition, the model underestimates the column density of DME and over-estimates that of acetaldehyde (AA, CH_3CHO) which we measured in HOPS-108. This can be seen in our observational results, where the AA column density is almost an order of magnitude lower than that of DME.

It is worth noting that a low DME/MF ratio was recently observed in two hot cores by [Law et al. \(2021\)](#). While it was not clear if the different trend is due to a higher gas temperature or if it is specific to hot core-like environments, these authors have suggested that an additional formation pathway of HCOOCH_3 can explain their results (see their Sect. 5.2.1). Supposing that the CH_3OCH_3 is forming via ice conversion independently of the temperature, they suggested that sufficiently efficient gas-phase

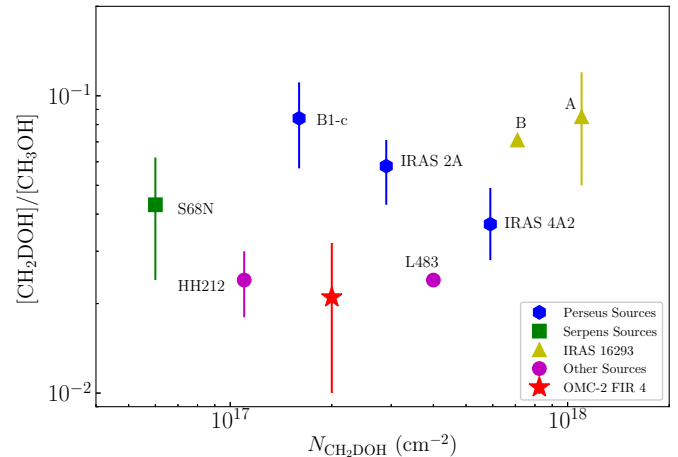


Fig. 6. Abundance ratio of CH_2DOH with respect to CH_3OH in HOPS-108 compared to isolated hot corinos where the CH_3OH column density was derived using one of its secondary isotopologues (see Sect. 4.2.2). All the sources are Class 0: IRAS 2A, IRAS 4A2 ([Taquet et al. 2015, 2019](#)), B1-c, S68N ([van Gelder et al. 2020](#)), HH212 ([Bianchi et al. 2017](#)), L483 ([Jacobsen et al. 2019](#)), IRAS 16293 A ([Manigand et al. 2020](#)), IRAS 16293 B ([Jørgensen et al. 2016, 2018](#)), and HOPS-108 in OMC-2 FIR 4 (this work).

reactions driving the extra production of HCOOCH_3 can explain the different ratios seen in hot cores. A similar result was also observed in the hot corino BHR 71 by [Yang et al. \(2020\)](#), but no discussion on iCOM column density ratios is reported.

In a nutshell, our DME/MF abundance ratio cannot be explained by either grain-surface or by gas-phase routes with our current knowledge. This highlights the need to theoretically revise the reaction network leading to or destroying MF and DME, and more generally iCOMs, including their rate coefficients. In addition, so far, the DME/MF ratio in hot corinos located in massive star-forming environments such as Orion have only been measured towards HOPS-108. Thus, further observations towards Orion hot corinos are needed to understand whether this low ratio is a consequence of the environmental conditions or a unique property of HOPS-108.

4.2.2. Methanol deuteration

The other noteworthy result obtained is for CH_2DOH . Figure 6 shows the abundance ratios of CH_2DOH with respect to CH_3OH . In this plot, all the data belong to Class 0 sources for which the CH_3OH column density was derived using $\text{CH}_3^{18}\text{OH}$ or $^{13}\text{CH}_3\text{OH}$. The deuteration ratios vary between $\sim 2\%$ and 9% . The lowest percentages ($\sim 2\%$) belong to HH212, HOPS-108, and L483. HH212 and HOPS-108 are both located in the Orion molecular complex. On the other hand, L483 is a hybrid source ([Oya et al. 2017](#)), that is with features from both a hot corino and warm carbon chain chemistry object (WCCC; [Sakai & Yamamoto 2013](#)), the latter being characterised by a lower deuteration compared to hot corinos. The highest percentages are seen in IRAS 16293 A, as well as IRAS 16293 B located in the Ophiuchus star-forming region and in B1-c located in Perseus. Arguably, the $[\text{CH}_2\text{DOH}]/[\text{CH}_3\text{OH}]$ ratio in HOPS-108 is within the typical hot corino values, even though it is at the lower end. Given that the majority of the molecules we observed in hot corinos are the result of ice mantle sublimation, the lower deuteration in HOPS-108 could be due to different physical conditions in the gas at the time when ice mantles were forming. Indeed,

methanol deuteration is strongly dependent on density, temperature, and time, and on the atomic D/H ratio in the gas phase during ice formation. Hence, as for HH212, the low deuteration ratio in HOPS-108 can provide us with a hint on the past physical conditions in the gas of the parental cloud during ice formation. Being in a more active star-forming region near high-mass stars that heat the gas, the lower deuteration in HOPS-108 can be due to a higher gas temperature in the early stages that decreases the atomic D/H ratio and consequently diminishes the methanol deuteration (Bianchi et al. 2017; Taquet et al. 2012, 2014, 2019).

Nevertheless, we stress that the column density of CH₂DOH in our work was derived using a single line and is thus subject to uncertainty. Therefore, more observations are needed to constrain the value we obtained.

5. Conclusions

In this work we studied iCOMs in HOPS-108, a Class 0 protostar located in the protocluster OMC-2 FIR 4, using ALMA at 1.2 mm and an angular resolution of $\sim 0''.28$ (~ 110 au). Our main conclusions are summarised as follows:

1. We detected 11 iCOMs with compact emission and high upper level energies (39 K–537 K). The molecular and continuum emission in this source are coincident and it originates from ~ 50 au scale and the kinetic temperature is found to be ≥ 120 K, confirming that HOPS-108 is a hot corino;
2. The kinetic temperature was derived using non-LTE analysis of CH₃¹⁸OH and CH₃OH lines. From this analysis, we found that CH₃OH lines are very optically thick ($\tau \sim 21$), which is probably also the case in other hot corinos. Hence, in similar studies of these sources, the column densities obtained from the main CH₃OH isotopologue are likely underestimated;
3. The HCOOCH₃ abundance relative to CH₃OH in HOPS-108 is ~ 3 – 5 times higher compared to that in other hot corinos where the CH₃OH column density was derived using one of its isotopologues. This indicates that HCOOCH₃ is likely enhanced in our source;
4. The N-bearing molecules abundance ratio with respect to HCOOCH₃ in HOPS-108 are lower than in other hot corinos, suggesting that HCOOCH₃ might be marginally enhanced relative to this family of molecules in this source;
5. The noticeable result in our study is the [CH₃OCH₃]/[HCOOCH₃] abundance ratio of $\sim 20\%$ which is lower in HOPS-108 than in other hot corinos, marginally deviating from the well-known correlation between the two molecules. Interestingly, this low ratio has also been recently observed in two hot cores. This might be due to local environmental effects; however, with the current chemical network, there is no suitable model that can explain this ratio;
6. We obtained a [CH₂DOH]/[CH₃OH] abundance ratio of $\sim 2\%$, which is relatively low with respect to the measured values in Perseus and Ophiuchus. This might result from higher temperatures of the parental molecular cloud at its early evolutionary stages due to high-mass star formation activity in the vicinity.

Our study highlights the importance of improving the chemical networks using theoretical calculations. It also suggests that more observations of CH₂DOH are needed to better constrain the deuteration in HOPS-108, and that more hot corinos located in dense clusters should be targeted to assess whether the observed abundance ratios are an environmental product or if HOPS-108 is an exceptional hot corino overall.

Acknowledgements. We thank the anonymous referee for careful reading and fruitful comments that helped to improve the paper. This project has received funding from the European Union's Horizon 2020 research and innovation program under the Marie Skłodowska-Curie grant agreement No 811312 for the Project "Astro-Chemical Origins" (ACO). This paper makes use of the following ALMA data: ADS/JAO.ALMA 2016.1.00376.S. ALMA is a partnership of ESO (representing its member states), NSF (USA) and NINS (Japan), together with NRC (Canada), MOST and ASIAA (Taiwan), and KASI (Republic of Korea), in cooperation with the Republic of Chile. The Joint ALMA Observatory is operated by ESO, AUI/NRAO and NAOJ. We thank Paola Caselli, Francesco Fontani and Valerio Lattanzi for useful discussions. C.Co. and L.P. acknowledge the project PRIN-INAF 2016 The Cradle of Life – GENESIS-SKA (General Conditions in Early Planetary Systems for the rise of life with SKA). C.F. acknowledges support from the French National Research Agency in the framework of the Investissements d'Avenir program (ANR-15-IDEX-02), through the funding of the "Origin of Life" project of the Univ. Grenoble-Alpes. A.L.S., C.C., C.Co, M.B., E.B. and C.F. acknowledge the funding from the European Research Council (ERC) under the European Union's Horizon 2020 research and innovation program, for the Project "The Dawn of Organic Chemistry" (DOC), grant agreement no. 741002.

References

- Adams, F. C. 2010, *ARA&A*, 48, 47
- Ascenzi, D., Cernuto, A., Balucani, N., et al. 2019, *A&A*, 625, A72
- Balucani, N., Ceccarelli, C., & Taquet, V. 2015, *MNRAS*, 449, L16
- Belloche, A., Maury, A. J., Maret, S., et al. 2020, *A&A*, 635, A198
- Bergner, J. B., Martín-Doménech, R., Öberg, K. I., et al. 2019, *ACS Earth Space Chem.*, 3, 1564
- Bianchi, E., Codella, C., Ceccarelli, C., et al. 2017, *A&A*, 606, A7
- Bianchi, E., Codella, C., Ceccarelli, C., et al. 2019, *MNRAS*, 483, 1850
- Bianchi, E., Chandler, C. J., Ceccarelli, C., et al. 2020, *MNRAS*, 498, L87
- Brouillet, N., Despois, D., Baudry, A., et al. 2013, *A&A*, 550, A46
- Calcutt, H., Jørgensen, J. K., Müller, H. S. P., et al. 2018, *A&A*, 616, A90
- Caselli, P., & Ceccarelli, C. 2012, *A&ARv*, 20, 56
- Ceccarelli, C. 2004, in *ASP Conf. Ser.*, 323, *Star Formation in the Interstellar Medium: In Honor of David Hollenbach*, eds. D. Johnstone, F. C. Adams, D. N. C. Lin, D. A. Neufeld, & E. C. Ostriker, 195
- Ceccarelli, C., Maret, S., Tielens, A. G. G. M., Castets, A., & Caux, E. 2003, *A&A*, 410, 587
- Ceccarelli, C., Caselli, P., Herbst, E., Tielens, A. G. G. M., & Caux, E. 2007, in *Protostars and Planets V*, eds. B. Reipurth, D. Jewitt, & K. Keil, 47
- Ceccarelli, C., Dominik, C., López-Sepulcre, A., et al. 2014, *ApJ*, 790, L1
- Ceccarelli, C., Caselli, P., Fontani, F., et al. 2017, *ApJ*, 850, 176
- Ceccarelli, C., Favre, C., López-Sepulcre, A., & Fontani, F. 2019, *Philos. Trans. R. Soc. Lond. A*, 377, 20180403
- Crimier, N., Ceccarelli, C., Lefloch, B., & Faure, A. 2009, *A&A*, 506, 1229
- Dubernet, M. L., Alexander, M. H., Ba, Y. A., et al. 2013, *A&A*, 553, A50
- Favre, C., López-Sepulcre, A., Ceccarelli, C., et al. 2017, *A&A*, 608, A82
- Favre, C., Ceccarelli, C., López-Sepulcre, A., et al. 2018, *ApJ*, 859, 136
- Fontani, F., Ceccarelli, C., Favre, C., et al. 2017, *A&A*, 605, A57
- Furlan, E., Megeath, S. T., Osorio, M., et al. 2014, *ApJ*, 786, 26
- Furlan, E., Fischer, W. J., Ali, B., et al. 2016, *ApJS*, 224, 5
- González-García, B., Manoj, P., Watson, D. M., et al. 2016, *A&A*, 596, A26
- Gounelle, M., Chaussidon, M., & Rollion-Bard, C. 2013, *ApJ*, 763, L33
- Green, S. 1986, *ApJ*, 309, 331
- Grossschedl, J. E., Alves, J., Meingast, S., et al. 2018, *VizieR Online Data Catalog: J/A+A/619/A106*
- Herbst, E., & van Dishoeck E. F. 2009, *ARA&A*, 47, 427
- Imai, M., Sakai, N., Oya, Y., et al. 2016, *ApJ*, 830, L37
- Jaber, A. A., Ceccarelli, C., Kahane, C., & Caux, E. 2014, *ApJ*, 791, 29
- Jacobsen, S. K., Jørgensen, J. K., Di Francesco, J., et al. 2019, *A&A*, 629, A29
- Jin, M., & Garrod, R. T. 2020, *ApJS*, 249, 26
- Jørgensen, J. K., van der Wiel, M. H. D., Coutens, A., et al. 2016, *A&A*, 595, A117
- Jørgensen, J. K., Müller, H. S. P., Calcutt, H., et al. 2018, *A&A*, 620, A170
- Jørgensen, J. K., Belloche, A., & Garrod, R. T. 2020, *ARA&A*, 58, 727
- Kahane, C., Jaber Al-Edhari, A., Ceccarelli, C., et al. 2018, *ApJ*, 852, 130
- Kainulainen, J., Stutz, A. M., Stanke, T., et al. 2017, *A&A*, 600, A141
- Kama, M., López-Sepulcre, A., Dominik, C., et al. 2013, *A&A*, 556, A57
- Kama, M., Caux, E., López-Sepulcre, A., et al. 2015, *A&A*, 574, A107
- Law, C. J., Zhang, Q., Öberg, K. I., et al. 2021, *ApJ*, 909, 214
- Lee, C.-F., Codella, C., Li, Z.-Y., & Liu, S.-Y. 2019, *ApJ*, 876, 63
- López-Sepulcre, A., Kama, M., Ceccarelli, C., et al. 2013a, *A&A*, 549, A114
- López-Sepulcre, A., Taquet, V., Sánchez-Monge, Á., et al. 2013b, *A&A*, 556, A62

- López-Sepulcre, A., Sakai, N., Neri, R., et al. 2017, [A&A](#), **606**, [A121](#)
- Lykke, J. M., Coutens, A., Jørgensen, J. K., et al. 2017, [A&A](#), **597**, [A53](#)
- Manigand, S., Jørgensen, J. K., Calcutt, H., et al. 2020, [A&A](#), **635**, [A48](#)
- Marcelino, N., Gerin, M., Cernicharo, J., et al. 2018, [A&A](#), **620**, [A80](#)
- Maret, S., Hily-Blant, P., Pety, J., Bardeau, S., & Reynier, E. 2011, [A&A](#), **526**, [A47](#)
- McMullin, J. P., Waters, B., Schiebel, D., Young, W., & Golap, K. 2007, in [ASP Conf. Ser.](#), **376**, [Astronomical Data Analysis Software and Systems XVI](#), eds. R. A. Shaw, F. Hill, & D. J. Bell, 127
- Megeath, S. T., Gutermuth, R., Muzerolle, J., et al. 2012, [AJ](#), **144**, [192](#)
- Mezger, P. G., Wink, J. E., & Zylka, R. 1990, [A&A](#), **228**, [95](#)
- Müller, H. S. P., Thorwirth, S., Roth, D. A., & Winnewisser, G. 2001, [A&A](#), **370**, [L49](#)
- Müller, H. S. P., Schlöder, F., Stutzki, J., & Winnewisser, G. 2005, [J. Mol. Struct.](#), **742**, [215](#)
- Nazari, P., van Gelder, M. L., van Dishoeck, E. F., et al. 2021, [A&A](#), **650**, [A150](#)
- Osorio, M., Díaz-Rodríguez, A. K., Anglada, G., et al. 2017, [ApJ](#), **840**, [36](#)
- Oya, Y., Sakai, N., Watanabe, Y., et al. 2017, [ApJ](#), **837**, [174](#)
- Pfalzner, S., Davies, M. B., Gounelle, M., et al. 2015, [Phys. Scr.](#), **90**, [068001](#)
- Pickett, H. M., Poynter, R. L., Cohen, E. A., et al. 1998, [J. Quant. Spec. Radiat. Transf.](#), **60**, [883](#)
- Rabli, D., & Flower, D. R. 2010, [MNRAS](#), **406**, [95](#)
- Sakai, N., & Yamamoto, S. 2013, [Chem. Rev.](#), **113**, [8981](#)
- Schöier, F. L., van der Tak, F. F. S., van Dishoeck, E. F., & Black, J. H. 2005, [A&A](#), **432**, [369](#)
- Shimajiri, Y., Takahashi, S., Takakuwa, S., Saito, M., & Kawabe, R. 2008, [ApJ](#), **683**, [255](#)
- Taquet, V., Ceccarelli, C., & Kahane, C. 2012, [A&A](#), **538**, [A42](#)
- Taquet, V., Charnley, S. B., & Sipilä, O. 2014, [ApJ](#), **791**, [1](#)
- Taquet, V., López-Sepulcre, A., Ceccarelli, C., et al. 2015, [ApJ](#), **804**, [81](#)
- Taquet, V., Bianchi, E., Codella, C., et al. 2019, [A&A](#), **632**, [A19](#)
- Tobin, J. J., Megeath, S. T., van't Hoff, M., et al. 2019, [ApJ](#), **886**, [6](#)
- van Gelder, M. L., Tabone, B., Tychoniec, Ł., et al. 2020, [A&A](#), **639**, [A87](#)
- Wilson, T. L., & Rood, R. 1994, [ARA&A](#), **32**, [191](#)
- Yang, Y.-L., Evans, Neal J., I., Smith, A., et al. 2020, [ApJ](#), **891**, [61](#)
- Yang, Y.-L., Sakai, N., Zhang, Y., et al. 2021, [ApJ](#), **910**, [20](#)

Appendix A: Line Parameters

Table A.1. List of transitions and line parameters used in this work.

Molecule	Transition	ν^a (GHz)	E_{up}^a (K)	g_{up}^a	A_{ij}^a (10^{-5} s^{-1})	FWHM ^b (km s ⁻¹)	T_{peak}^b (K)	Line flux ^b (K km s ⁻¹)	V_{peak}^b (km s ⁻¹)
HCOOCH ₃ ^c	20 _{17,3} – 19 _{17,2} A	245.5175	315.5	82	6.23	3.2 ± 0.4	4.29	14.6 ± 0.3	12.2 ± 0.2
HCOOCH ₃ ^c	20 _{17,4} – 19 _{17,3} A	245.5175	315.5	82	6.23				
HCOOCH ₃	20 _{15,5} – 19 _{15,4} E	245.6567	273.1	82	9.83	2.7 ± 0.1	4.25	12.3 ± 0.4	12.3 ± 0.1
HCOOCH ₃	20 _{15,6} – 19 _{15,5} E	245.6729	273.1	82	9.84	2.6 ± 0.1	5.02	13.8 ± 0.5	12.3 ± 0.1
HCOOCH ₃ ^c	20 _{14,6} – 19 _{14,5} A	245.7522	253.9	82	11.5	4.1 ± 0.1	7.54	32.8 ± 0.5	11.2 ± 0.1
HCOOCH ₃ ^c	20 _{14,7} – 19 _{14,6} A	245.7522	253.9	82	11.5				
HCOOCH ₃	20 _{14,7} – 19 _{14,6} E	245.7726	253.9	82	11.5	2.7 ± 0.1	6.64	18.9 ± 0.5	12.6 ± 0.1
HCOOCH ₃	21 _{4,18} – 20 _{3,17} E	246.0275	139.8	86	2.37	2.6 ± 0.1	4.08	11.1 ± 0.4	12.4 ± 0.1
HCOOCH ₃	21 _{2,19} – 20 _{3,18} E	246.0388	139.8	86	2.37	2.5 ± 0.1	4.38	11.7 ± 0.4	12.5 ± 0.1
HCOOCH ₃	20 _{11,9} – 19 _{11,8} E	246.2854	204.2	82	15.8	2.8 ± 0.2	6.05	18.3 ± 0.7	12.4 ± 0.1
HCOOCH ₃ ^c	20 _{11,10} – 19 _{11,9} A	246.2951	204.2	82	15.8	3.2 ± 0.3	7.91	27.3 ± 1.8	12.6 ± 0.1
HCOOCH ₃ ^c	20 _{11,9} – 19 _{11,8} A	246.2951	204.2	82	15.8				
HCOOCH ₃	20 _{11,10} – 19 _{11,9} E	246.3082	204.2	82	15.8	2.8 ± 0.1	6.14	18.0 ± 0.7	12.3 ± 0.1
HCOOCH ₃	22 _{1,21} – 21 _{1,20} A, $\nu_t = 1$	246.4884	330.4	90	22.2	2.7 ± 0.1	4.86	13.8 ± 0.4	12.3 ± 0.1
HCOOCH ₃	20 _{10,11} – 19 _{10,10} E	246.6231	190.3	82	17.4	2.6 ± 0.1	7.04	19.4 ± 0.7	12.3 ± 0.1
HCOOCH ₃	15 _{4,12} – 14 _{3,11} A	246.6834	81.8	62	1.17	2.8 ± 0.5	3.12	9.3 ± 1.3	12.4 ± 1.2
HCOOCH ₃	22 _{2,21} – 21 _{2,20} E, $\nu_t = 1$	246.7065	329.9	90	22.3	2.7 ± 0.2	4.28	12.2 ± 0.6	12.4 ± 0.1
HCOOCH ₃	22 _{1,21} – 21 _{1,20} E, $\nu_t = 1$	246.7317	329.9	90	22.3	2.7 ± 0.1	5.22	14.8 ± 0.5	12.3 ± 0.1
HCOOCH ₃	10 _{5,5} – 9 _{4,5} E	246.7529	49.1	42	1.25	2.2 ± 0.2	2.78	6.4 ± 0.7	12.3 ± 0.1
HCOOCH ₃	19 _{2,17} – 18 _{2,16} E	246.8916	126.2	78	21.8	3.3 ± 0.1	8.02	27.9 ± 0.7	12.4 ± 0.1
HCOOCH ₃	19 _{4,15} – 18 _{4,14} A	246.9146	126.2	78	21.8	3.0 ± 0.1	8.15	26.3 ± 0.8	12.3 ± 0.1
HCOOCH ₃	10 _{5,6} – 9 _{4,6} E	246.9457	49.1	42	1.26	2.4 ± 0.2	3.41	8.7 ± 0.7	12.2 ± 0.1
HCOOCH ₃	20 _{6,15} – 19 _{6,14} A, $\nu_t = 1$	246.9852	335.4	82	20.7	2.4 ± 0.1	4.85	12.4 ± 0.6	12.4 ± 0.1
HCOOCH ₃	20 _{9,12} – 19 _{9,11} E	247.0636	177.8	82	18.2	2.7 ± 0.1	6.77	19.7 ± 0.9	12.2 ± 0.1
HCOOCH ₃	10 _{5,5} – 9 _{4,6} A	247.1242	49.1	42	1.82	3.1 ± 0.3	3.20	10.5 ± 0.5	12.4 ± 0.1
HCOOCH ₃	20 _{9,11} – 20 _{8,12} E	231.9552	177.8	82	1.56	2.5 ± 0.5	2.28	6.1 ± 1.0	12.1 ± 0.2
HCOOCH ₃	19 _{9,10} – 19 _{8,11} A	232.6172	166.0	78	1.53	2.2 ± 0.3	3.15	7.5 ± 0.8	12.2 ± 0.2
HCOOCH ₃	19 _{9,11} – 19 _{8,12} A	232.6252	166.0	78	1.53	2.4 ± 0.3	2.77	7.1 ± 0.8	12.4 ± 0.2
HCOOCH ₃	19 _{10,10} – 18 _{10,9} E, $\nu_t = 1$	232.6839	365.5	78	13.8	2.2 ± 0.3	3.19	7.4 ± 0.8	12.4 ± 0.1
HCOOCH ₃	19 _{8,11} – 18 _{8,10} E, $\nu_t = 1$	232.7386	342.0	78	15.7	2.0 ± 0.3	4.07	8.7 ± 1.0	12.4 ± 0.1
HCOOCH ₃	19 _{8,11} – 18 _{8,10} A, $\nu_t = 1$	232.8396	341.8	78	15.7	2.4 ± 0.3	3.32	8.5 ± 0.9	12.3 ± 0.1
CH ₃ OH	18 _{3,16} – 17 _{4,13} A	232.7834	446.5	148	2.17	3.5 ± 0.2	6.94	26.2 ± 1.3	12.4 ± 0.1
CH ₃ OH	10 _{-3,8} – 11 _{-2,10} E	232.9457	190.4	84	2.13	4.3 ± 0.2	9.50	43.1 ± 1.6	12.7 ± 0.1
CH ₃ OH	19 _{3,16} – 19 _{2,17} E	246.8733	490.7	156	8.27	4.2 ± 0.1	11.24	49.8 ± 0.7	12.4 ± 0.1
CH ₃ ¹⁸ OH ^d	5 _{-1,5} – 4 _{-1,4} E	231.7358	39.0	44	5.13	4.3 ± 0.8	1.75	8.0 ± 1.3	12.1 ± 0.4
CH ₃ ¹⁸ OH ^{c,d,*}	5 _{3,2} – 4 _{3,1} E	231.8013	81.3	44	3.42	3.8 ± 0.8	2.69	10.9 ± 1.8	11.4 ± 0.4
CH ₃ ¹⁸ OH ^{c,d,*}	5 _{2,4} – 4 _{2,3} A	231.8015	70.9	44	4.53				
CH ₃ ¹⁸ OH	5 _{1,4} – 4 _{1,3} E	231.8267	54.1	44	5.33	2.7 ± 0.7	1.46	4.1 ± 0.9	12.3 ± 0.3
CH ₃ ¹⁸ OH ^e	5 _{-2,4} – 4 _{-2,3} E	231.8538	59.2	44	4.49	3.8 ± 1.1	1.40	5.6 ± 1.3	10.5 ± 0.4
CH ₃ ¹⁸ OH	5 _{2,3} – 4 _{2,2} E	231.8645	55.8	44	4.41	3.5 ± 0.8	1.30	4.9 ± 1.0	11.3 ± 0.4
CH ₂ DOH	4 _{1,4} – 4 _{1,3} E1	246.9731	37.7	9	2.15	2.9 ± 0.2	3.48	10.6 ± 0.6	12.4 ± 0.1
CH ₃ OCH ₃ ^{c,d,e}	13 _{0,13} – 12 _{1,12} AA	231.9878	80.9	270	9.15				
CH ₃ OCH ₃ ^{c,d,e}	13 _{0,13} – 12 _{1,12} EE	231.9879	80.9	432	9.15	2.9 ± 0.2	6.52	20.3 ± 1.1	12.3 ± 0.1
CH ₃ OCH ₃ ^{c,d,e}	13 _{0,13} – 12 _{1,12} AE	231.9879	80.9	162	9.15				
CH ₃ OCH ₃ ^{c,d,e}	13 _{0,13} – 12 _{1,12} EA	231.9879	80.9	108	9.15				
CH ₃ OCH ₃ ^f	17 _{5,12} – 17 _{4,13} AE	259.3094	174.5	140	8.74	2.1 ± 0.3	3.83	8.6 ± 1.1	12.2 ± 0.1
CH ₃ OCH ₃ ^f	17 _{5,12} – 17 _{4,13} EA	259.3097	174.5	140	8.74				
CH ₃ OCH ₃ ^f	17 _{5,12} – 17 _{4,13} EE	259.3119	174.5	560	8.76	1.6 ± 0.2	5.20	9.0 ± 1.0	12.1 ± 0.1
CH ₃ COCH ₃ ^c	21 _{4,17} – 20 _{5,16} AE	245.2965	145.1	258	53.9				
CH ₃ COCH ₃ ^c	21 _{5,17} – 20 _{4,16} AE	245.2965	145.1	86	53.9	2.8 ± 0.9	1.85	5.4 ± 1.4	12.5 ± 0.4
CH ₃ COCH ₃ ^c	21 _{4,17} – 20 _{5,16} EA	245.2965	145.1	172	53.9				
CH ₃ COCH ₃ ^c	21 _{5,17} – 20 _{4,16} EA	245.2965	145.1	172	53.9				
CH ₃ COCH ₃ ^c	21 _{4,17} – 20 _{5,16} AA	245.4095	145.0	430	53.9	2.8 ± 0.2	2.00	5.9 ± 0.5	12.4 ± 0.1
CH ₃ COCH ₃ ^c	21 _{5,17} – 20 _{4,16} AA	245.4095	145.0	258	53.9				

Continued on next page

Table A.1. –Continued

Molecule	Transition	ν^a (GHz)	E_{up}^a (K)	g_{up}^a	A_{ij}^a (10^{-5} s^{-1})	FWHM ^b (km s ⁻¹)	T_{peak}^b (K)	Line flux ^b (K km s ⁻¹)	V_{peak}^b (km s ⁻¹)
CH ₃ COCH ₃ ^c	22 _{3,19} –21 _{4,18} EE	246.4504	149.6	720	58.2				
CH ₃ COCH ₃ ^c	22 _{4,19} –21 _{4,18} EE	246.4504	149.6	720	1.2				
CH ₃ COCH ₃ ^c	22 _{3,19} –21 _{3,18} EE	246.4504	149.6	720	0.81	2.6 ± 0.1	3.64	10.3 ± 0.5	12.2 ± 0.1
CH ₃ COCH ₃ ^c	22 _{4,19} –21 _{3,18} EE	246.4504	149.6	720	58.6				
CH ₃ CHO ^d	12 _{3,10} –11 _{3,9} E	231.7487	92.5	50	39.4	3.9 ± 0.8	1.46	5.7 ± 0.9	12.4 ± 0.4
CH ₃ CHO ^d	12 _{3,9} –11 _{3,8} E	231.8475	92.6	50	39.4	3.1 ± 0.4	2.26	7.5 ± 1.0	13.1 ± 0.2
CH ₃ CN ^f	14 ₁ –13 ₁	257.5224	99.8	58	147	4.6 ± 0.1	18.2	89.2 ± 2.1	12.3 ± 0.1
CH ₃ CN ^f	14 ₀ –13 ₀	257.5274	92.7	58	148	3.9 ± 0.1	19.05	81.8 ± 2.7	12.3 ± 0.1
¹³ CH ₃ CN	13 ₃ –12 ₃	232.1949	142.4	108	102	2.5 ± 0.3	3.51	9.4 ± 1.1	12.5 ± 0.1
¹³ CH ₃ CN	13 ₁ –12 ₁	232.2298	85.2	54	107	2.4 ± 0.3	3.34	8.4 ± 1.1	12.2 ± 0.2
¹³ CH ₃ CN	13 ₀ –12 ₀	232.2341	78.0	54	108	2.4 ± 0.4	3.35	8.5 ± 1.3	12.3 ± 0.2
C ₂ H ₅ CN	26 _{3,24} –25 _{3,23}	232.7900	161.0	53	105	3.3 ± 0.8	1.44	5.0 ± 1.1	12.3 ± 0.4
C ₂ H ₅ CN ^c	26 _{10,16} –25 _{10,15}	232.9623	262.0	53	91.2				
C ₂ H ₅ CN ^c	26 _{10,17} –25 _{10,16}	232.9623	262.0	53	91.2	2.3 ± 0.6	1.98	4.8 ± 1.0	12.4 ± 0.2
C ₂ H ₅ CN ^c	26 _{9,17} –25 _{9,16}	232.9675	240.9	53	94.2				
C ₂ H ₅ CN ^c	26 _{9,18} –25 _{9,17}	232.9675	240.9	53	94.2	2.8 ± 0.7	1.61	4.8 ± 1.0	12.4 ± 0.3
C ₂ H ₅ CN ^c	26 _{11,15} –25 _{11,14}	232.9755	285.2	53	87.9				
C ₂ H ₅ CN ^c	26 _{11,16} –25 _{11,15}	232.9755	285.2	53	87.9	1.6 ± 1.0	2.15	3.7 ± 0.8	12.3 ± 0.1
C ₂ H ₅ CN ^c	26 _{8,19} –25 _{8,18}	232.9987	222.0	53	96.9				
C ₂ H ₅ CN ^c	26 _{8,18} –25 _{8,17}	232.9987	222.0	53	96.9	2.7 ± 0.4	2.29	6.7 ± 0.9	12.7 ± 0.2
C ₂ H ₅ CN ^c	26 _{7,20} –25 _{7,19}	233.0693	205.4	53	99.4				
C ₂ H ₅ CN ^c	26 _{7,19} –25 _{7,18}	233.0693	205.4	53	99.4	2.7 ± 0.5	2.73	7.8 ± 1.2	12.5 ± 0.3
NH ₂ CHO	11 _{2,10} –10 _{2,9}	232.2736	78.9	23	88.2	3.5 ± 0.4	2.56	9.6 ± 1.0	12.0 ± 0.2
NH ₂ CHO ^f	12 _{1,12} –11 _{1,11}	243.5210	79.2	25	105	1.7 ± 0.2	5.71	10.1 ± 0.9	13.0 ± 0.1

Notes:

^a The frequencies and spectroscopic parameters of HCOOCH₃, CH₂DOH, CH₃COCH₃, and CH₃CHO have been extracted from the JPL catalogue (Pickett et al. 1998). The frequencies and spectroscopic parameters of CH₃OH, CH₃¹⁸OH, CH₃OCH₃, CH₃CN, ¹³CH₃CN, C₂H₅CN, and NH₂CHO have been extracted from the CDMS catalogue (Müller et al. 2001, 2005).

^b Parameters and uncertainties determined by Gaussian fit.

^c The lines cannot be distinguished.

^d Estimated after subtracting the small contribution from HCOOCH₃.

^e Estimated after subtracting the small contribution from C₂H₅CN.

^f Lines from narrow spws (58.59 MHz) and different channel width (~ 0.15 km s⁻¹) (see Table. 1).

* The collisional coefficients have not been calculated for the E transition so we used only the A transition in the LVG. We assumed a flux value equal to 40% of the total line flux because the A transition would be less populated with respect to the E one given that it has lower E_{up} and A_{ij} . However, the result does not change much if we assume a value between 30% and 60% of the total flux.

Appendix B: Figures

For each studied molecule, we provide a sample of spectra of the detected lines. The transitions of CH_3CHO , CH_3OCH_3 , and $\text{CH}_3^{18}\text{OH}$ that were slightly contaminated by either HCOOCH_3 or $\text{C}_2\text{H}_5\text{CN}$ (by $<20\%$ of the total line flux) are reported together with the expected intensities of the contaminating lines. The corresponding intensities were obtained with the LTE model of the CLASS software using the column densities and rotational temperatures obtained in our analysis, and they were removed after from the CH_3CHO , CH_3OCH_3 , and $\text{CH}_3^{18}\text{OH}$ lines using the 'subtract' command in CLASS.

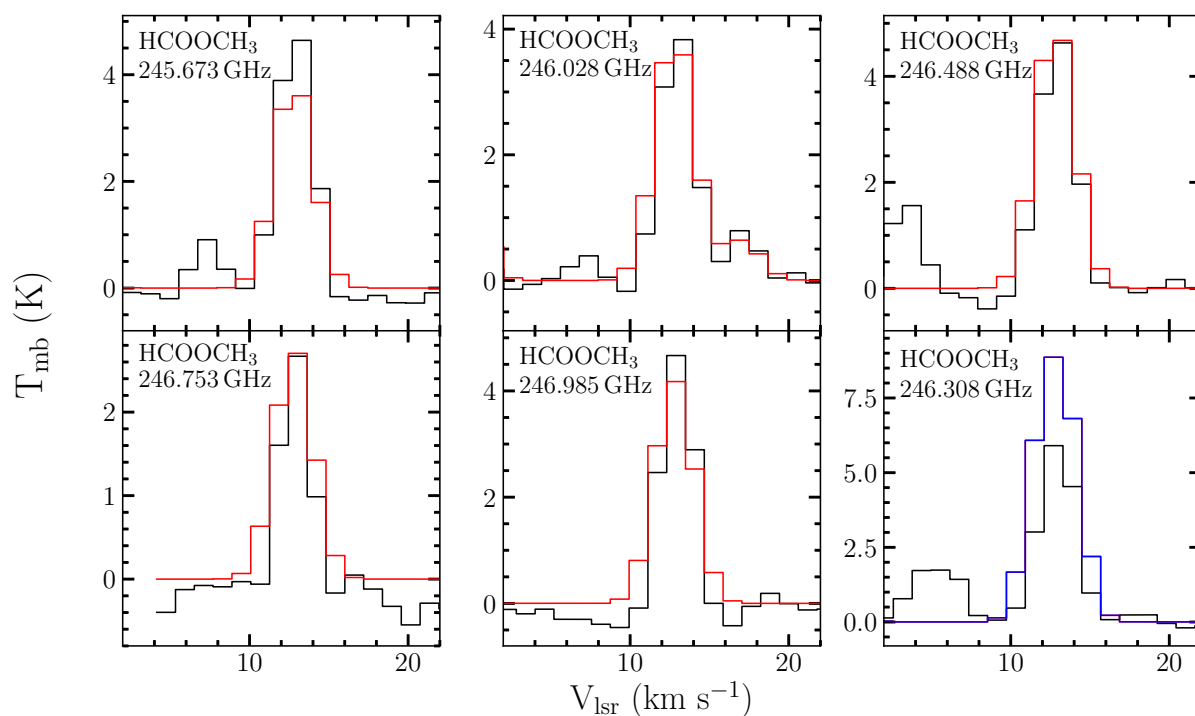


Fig. B.1. Sample of some observed HCOOCH_3 spectral lines towards HOPS-108 (black). The spectra predicted by the best-fit LTE model are depicted in red. The blue spectrum corresponds to the best-fit model prediction of an optically thick line, which was excluded from the analysis (see Sect. 3.4).

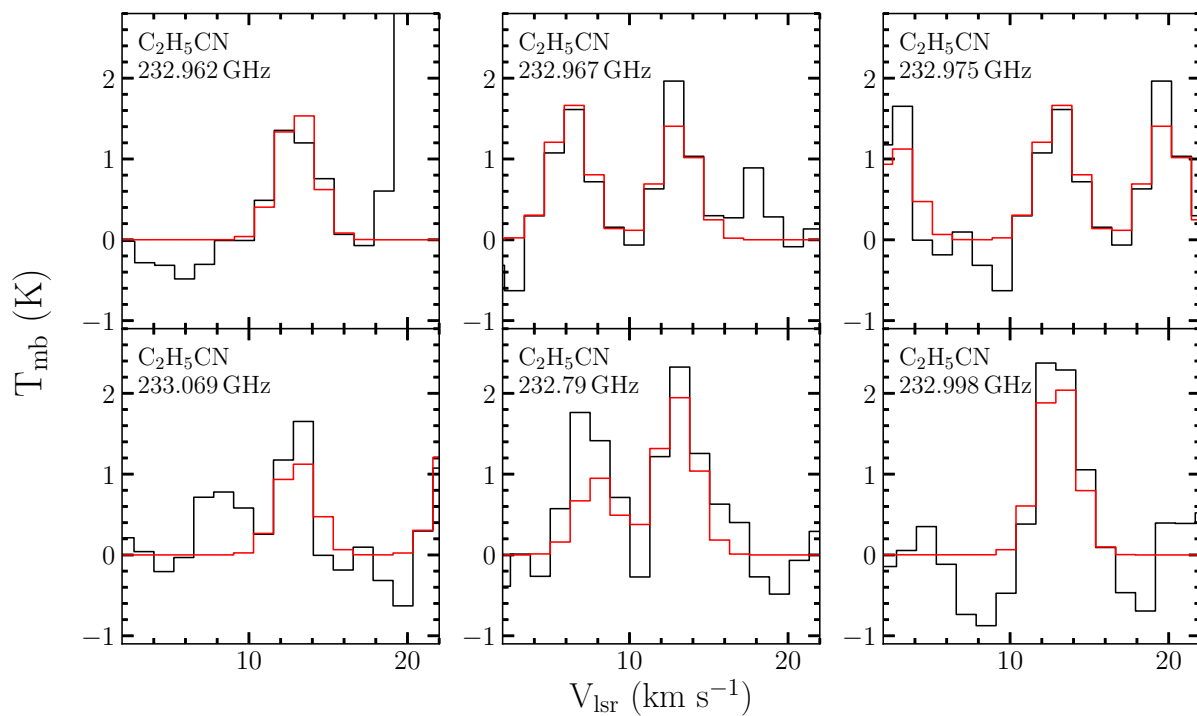


Fig. B.2. $\text{C}_2\text{H}_5\text{CN}$ observed spectral lines (black) towards HOPS-108, and the spectra predicted by the best-fit LTE model (red).

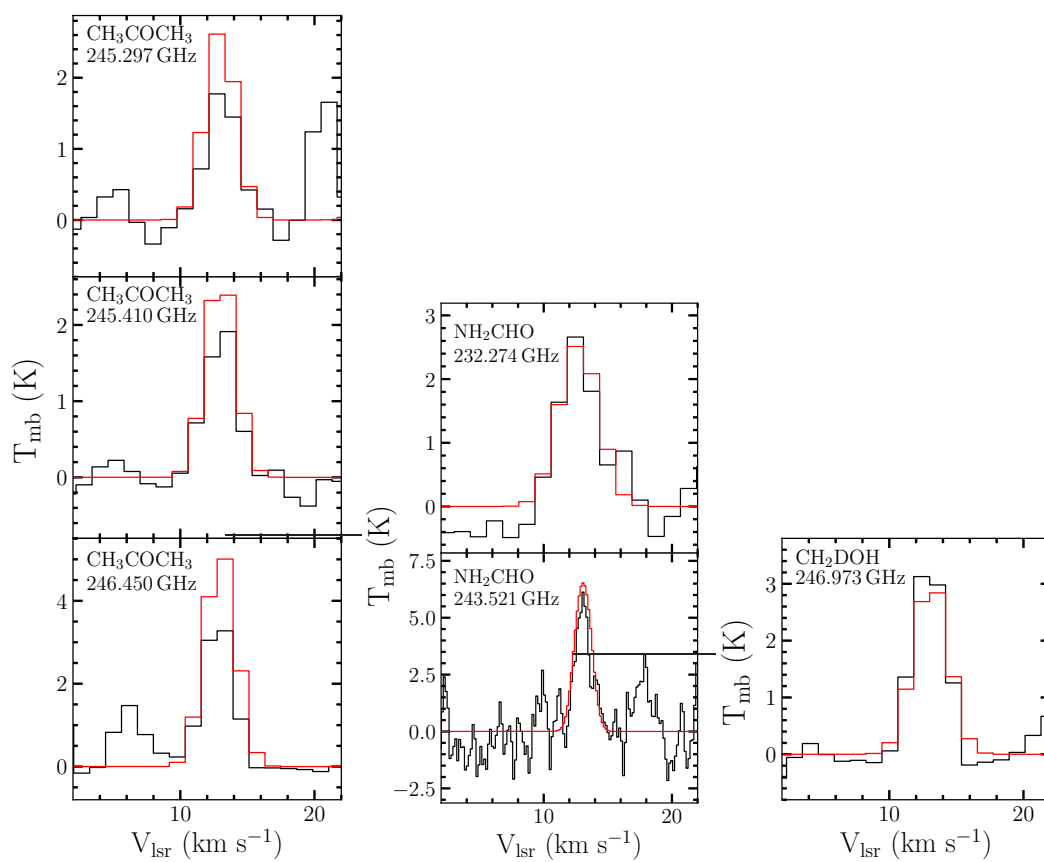


Fig. B.3. CH_3COCH_3 , NH_2CHO , and CH_2DOH observed spectral lines (black) towards HOPS-108. The spectra predicted by the best-fit LTE model are depicted in red.

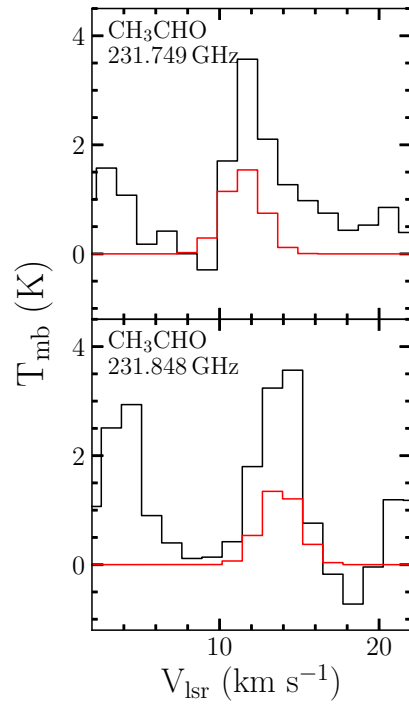


Fig. B.4. CH_3CHO observed spectral lines (black) towards HOPS-108. The contamination from HCOOCH_3 is shown in red.

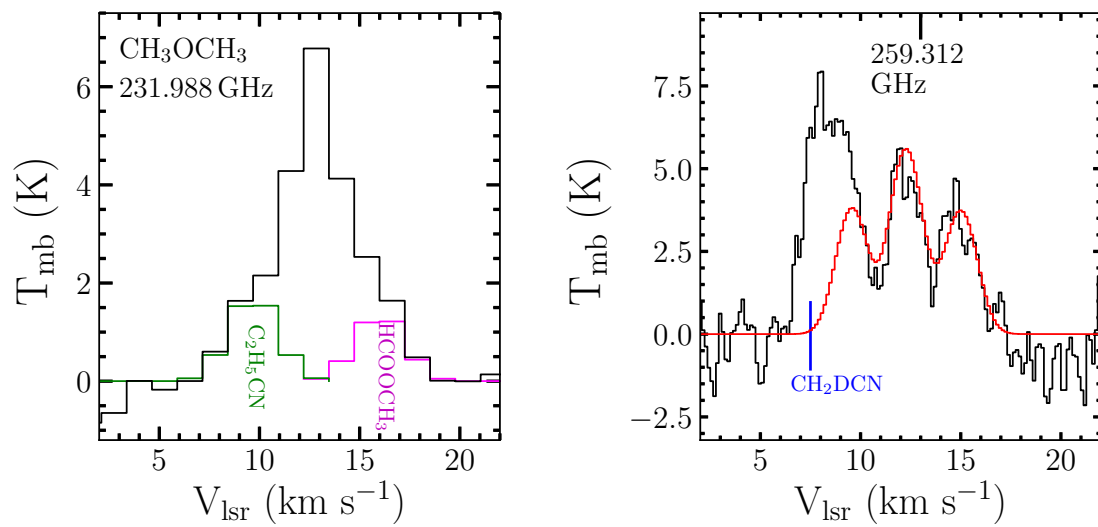


Fig. B.5. CH_3OCH_3 observed spectral lines (black) towards HOPS-108. Left: The contamination from HCOOCH_3 and $\text{C}_2\text{H}_5\text{CN}$ are shown in magenta and green, respectively. Right: The spectrum predicted by the best-fit LTE model is depicted in red.

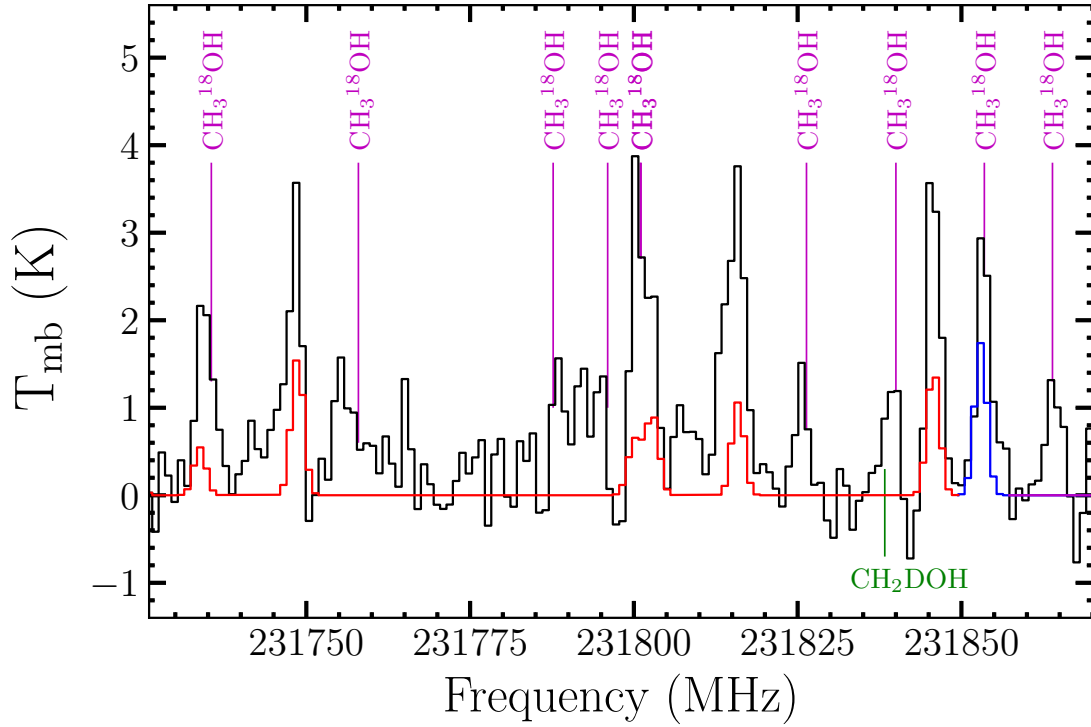


Fig. B.6. $\text{CH}_3^{18}\text{OH}$ observed spectral lines (black) towards HOPS-108. The contamination from HCOOCH_3 and $\text{C}_2\text{H}_3\text{CN}$ are shown in red and blue, respectively. The $\text{CH}_3^{18}\text{OH}$ lines are marked in magenta.

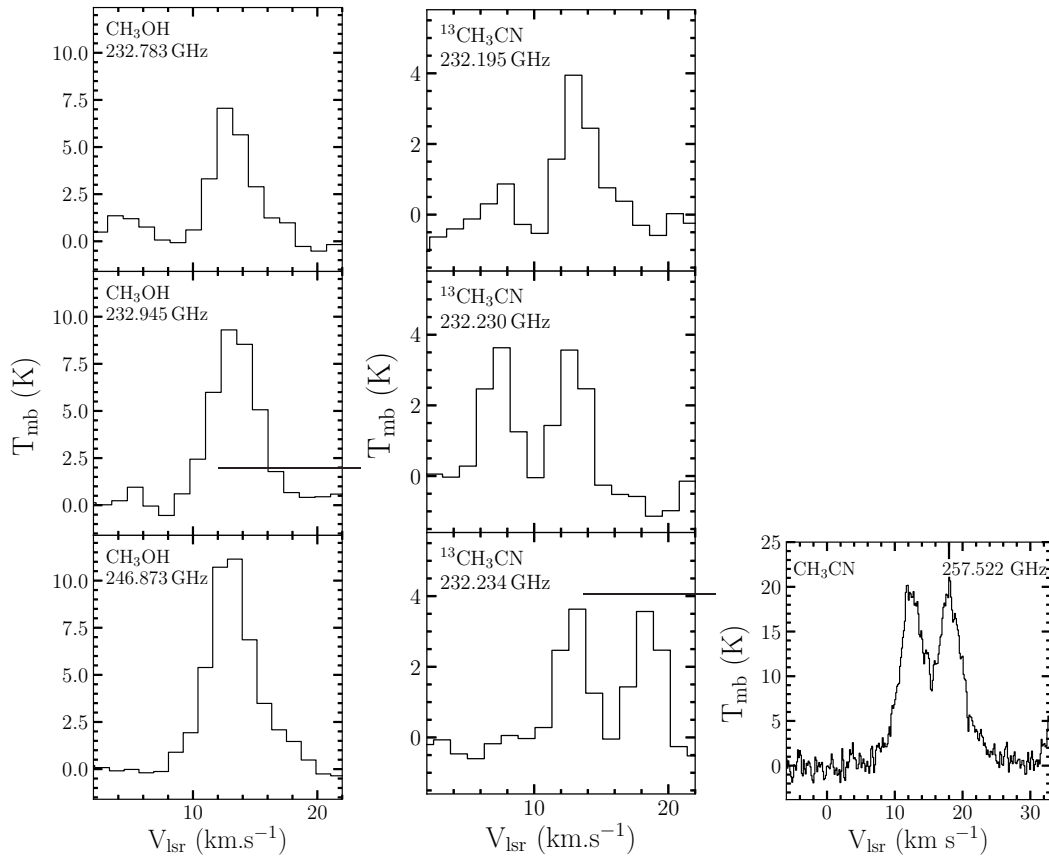


Fig. B.7. CH_3OH , $^{13}\text{CH}_3\text{CN}$, and CH_3CN observed spectral lines towards HOPS-108. The $^{13}\text{CH}_3\text{CN}$ and CH_3CN lines are used in the non-LTE analysis. Among the CH_3OH lines, only the one at 232.783 GHz was used in the non-LTE analysis.

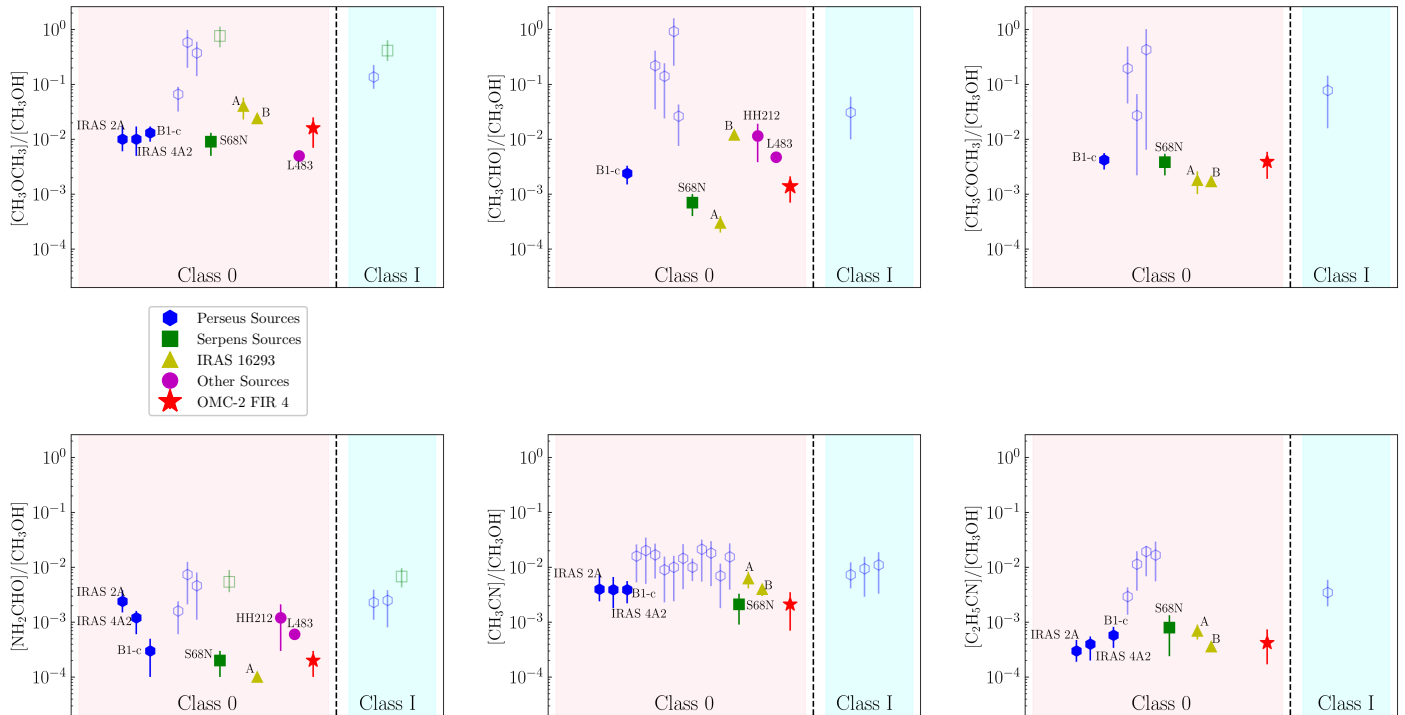


Fig. B.8. Abundance ratio of iCOMs with respect to CH_3OH in HOPS-108 compared to other isolated hot corinos. The sources are separated according to their class, with no particular order within a given class. The open symbols correspond to the sources where the CH_3OH column density is most likely underestimated due to its high optical depth (See Sect. 4.2.1). The Class 0 sources are: IRAS 2A, IRAS 4A2 (Taquet et al. 2015; López-Sepulcre et al. 2017), B1-c, S68N (van Gelder et al. 2020; Nazari et al. 2021), IRAS19347 + 0727 in B335 (Imai et al. 2016), HH212 (Bianchi et al. 2017; Lee et al. 2019), L483 (Jacobsen et al. 2019), Ser-emb 1 (Bergner et al. 2019), IRAS 16293 A (Manigand et al. 2020; Calcutt et al. 2018), IRAS 16293 B (Jørgensen et al. 2016, 2018; Lykke et al. 2017; Calcutt et al. 2018), HOPS-108 in OMC-2 FIR 4 (this work), and the sources from the PEACHES survey (Yang et al. 2021), including Per-emb 1, Per-emb 2, Per-emb 5, Per-emb 10, Per-emb 11A, Per-emb 11C, Per-emb 12, Per-emb 13, Per-emb 18, Per-emb 20, Per-emb 21, Per-emb 22A, Per-emb 22B, Per-emb 26, Per-emb 27, Per-emb 29, Per-emb 33A, L1448 IRS3A, L1448-NW, SVS-13B, and B1-bS. The Class I sources are: Ser-emb 17 (Bergner et al. 2019), L1551 (Bianchi et al. 2020), and also sources from the PEACHES survey (Yang et al. 2021), including Per-emb 35A, Per-emb 35B, Per-emb 42, Per-emb 44, Per-emb 53, and SVS13-A2. The same plots for HCOOCH_3 and CH_2DOH are represented in Figs. 4 and 6, respectively.

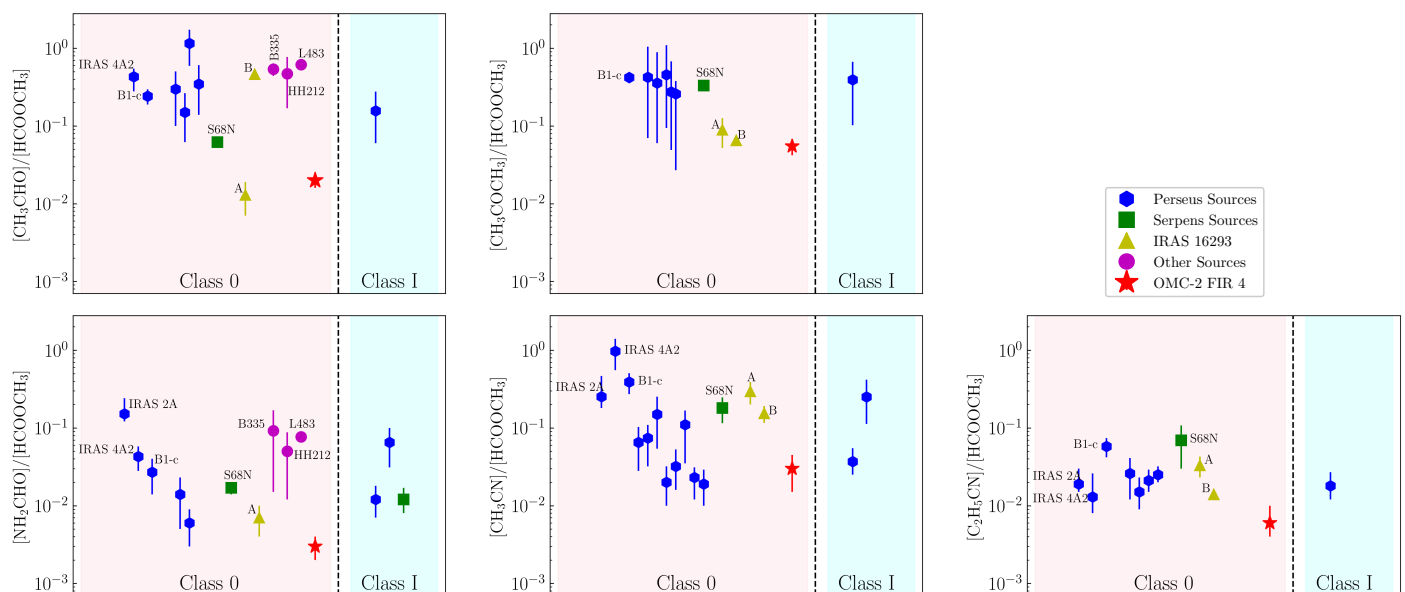


Fig. B.9. Abundance ratio of iCOMs with respect to HCOOCH_3 in HOPS-108 compared to other isolated hot corinos. The sources are separated according to their class, with no particular order within a given class. The same sources from Fig. B.8 are used. The same plot for CH_3OCH_3 is represented in Fig. 5.

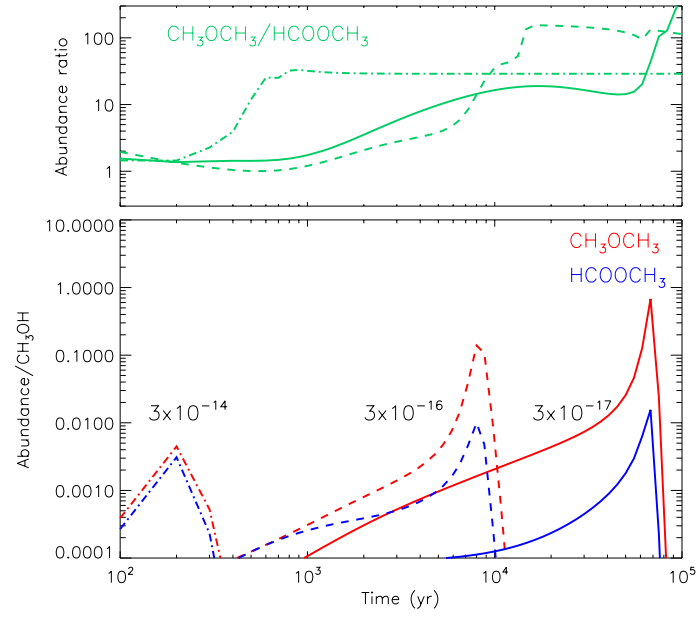


Fig. B.10. Top: $\text{CH}_3\text{OCH}_3/\text{HCOOCH}_3$ ratio as a function of time for different ionisation rate values (in units of s^{-1}). Bottom: CH_3OCH_3 and HCOOCH_3 abundances with respect to CH_3OH as a function of time for different ionisation rate values ζ . The ionisation rates in the upper and lower panel are the same: the solid lines correspond to $\zeta=3 \times 10^{-17} \text{ s}^{-1}$, the dashed lines correspond to $\zeta=3 \times 10^{-16} \text{ s}^{-1}$, and the dot-dashed lines correspond to $\zeta=3 \times 10^{-14} \text{ s}^{-1}$.